SPECTRAL ENERGY DISTRIBUTIONS OF HARD X-RAY SELECTED ACTIVE GALACTIC NUCLEI IN THE *XMM-NEWTON* MEDIUM DEEP SURVEY

M. POLLETTA,[1] M. TAJER,[2,3] L. MARASCHI,[2] G. TRINCHIERI,[2] C. J. LONSDALE,[1] L. CHIAPPETTI,[4]
S. ANDREON,[2] M. PIERRE,[5] O. LE FÈVRE,[6] G. ZAMORANI,[7] D. MACCAGNI,[4] O. GARCET,[8]
J. SURDEJ,[8] A. FRANCESCHINI,[9] D. ALLOIN,[5] D. L. SHUPE,[10] J. A. SURACE,[10] F. FANG,[10]
M. ROWAN-ROBINSON,[11] H. E. SMITH,[1] AND L. TRESSE[6]

ABSTRACT

We present the SEDs of a hard X-ray selected sample containing 136 sources with $F_{2-10\,\mathrm{keV}} > 10^{-14}$ erg cm^{-2} s^{-1}; 132 are AGNs. The sources are detected in a 1 deg^2 area of the *XMM-Newton* Medium Deep Survey where optical data from the VVDS and CFHTLS and infrared data from the SWIRE survey are available. Based on a SED fitting technique we derive photometric redshifts with $\sigma(1 + z) = 0.11$ and 6% of outliers and identify AGN signatures in 83% of the objects. This fraction is higher than derived when a spectroscopic classification is available. The remaining $17^{+9}_{-6}\%$ of AGNs show star-forming galaxy SEDs (SF class). The sources with AGN signatures are divided in two classes, AGN1 ($33^{+6}_{-1}\%$) and AGN2 ($50^{+6}_{-11}\%$). The AGN1 and AGN2 classes include sources whose SEDs are fitted by type 1 and type 2 AGN templates, respectively. On average, AGN1s show soft X-ray spectra, consistent with being unabsorbed, while AGN2s and SFs show hard X-ray spectra, consistent with being absorbed. The analysis of the average SEDs as a function of X-ray luminosity shows a reddening of the infrared SEDs, consistent with a decreasing contribution from the host galaxy at higher luminosities. The AGNs in the SF classes are likely obscured in the mid-infrared, as suggested by their low $L_{3-20\,\mu m}/L^{\mathrm{corr}}_{0.5-10\,\mathrm{keV}}$ ratios. We confirm the previously found correlation for AGNs between the radio luminosity and the X-ray and the mid-infrared luminosities. The X-ray–radio correlation can be used to identify heavily absorbed AGNs. However, the estimated radio fluxes for the missing AGN population responsible for the bulk of the background at $E > 10$ keV are too faint to be detected even in the deepest current radio surveys.

Subject headings: galaxies: active — infrared: galaxies — quasars: general — X-rays: galaxies

Online material: color figures

1. INTRODUCTION

Active galactic nuclei (AGNs) are mostly found in X-ray surveys, where they represent the majority of the detected population. However, some AGNs are missed even in the deepest X-ray observations, e.g., the *Chandra* Deep Surveys, CDFN (Brandt et al. 2001; Barger et al. 2002) and CDFS (Giacconi et al. 2002; Rosati et al. 2002). The existence of a large population of AGNs that is still undetected, even in the deepest X-ray surveys, is suggested by the unresolved X-ray background (Worsley et al. 2005) and by the discovery of AGNs not detected at X-ray energies but identified at radio and infrared wavelengths (Polletta et al. 2006; Higdon et al. 2005; Donley et al. 2005). Multiwavelength obser-

vations of AGNs are necessary to make a census of AGNs and to fully characterize them.

Current facilities and projects permit the study of large AGN samples throughout the entire wavelength spectrum, from radio wavelengths to X-ray energies. Several wide and deep multiwavelength surveys are currently being performed, providing enough area, coverage, and sensitivity to sample the multiwavelength properties of AGNs. A difficult task that multiwavelength surveys need to face is the identification of AGNs. AGNs usually represent only a small fraction of sources compared to the population detected at optical and IR wavelengths, and their properties can be elusive. Obscured AGNs can be elusive because their optical emission resembles that of normal galaxies and therefore they cannot be identified by the color-selection techniques used for QSOs (e.g., Schmidt & Green 1983), or because their spectra do not show any AGN signature. Their IR emission can be dominated by PAH features, typical of star-forming galaxies, instead of continuum emission from hot dust. Radio observations reveal the radio-loud population of obscured AGNs (e.g., radio galaxies), but this comprises only a small fraction, ~10%, of the total AGN population. A hard X-ray selection fails to detect the luminous narrow-line AGNs in the numbers predicted by some models of the cosmic X-ray background (CXRB).

In order to obtain a complete picture of the AGN population, selection biases need to be taken into account. The fraction of AGNs missed in observations in narrow energy windows, e.g., X-rays, infrared, or optical, is not well known. Moreover, the dispersion in the spectral energy distributions (SEDs) of all kinds of AGNs needs to be well characterized to evaluate which and what fraction of AGNs are missed in one wavelength window but

[1] Center for Astrophysics and Space Sciences, University of California, San Diego, La Jolla, CA 92093-0424.

[2] INAF–Osservatorio di Brera, via Brera 28, 20121 Milano, Italy.

[3] Università degli studi di Milano-Bicocca, Dipartimento di fisica, Piazza della Scienza 3, 20126 Milano, Italy.

[4] INAF–IASF Milano, via Bassini 15, I-20133 Milano, Italy.

[5] CEA Saclay, DSM/DAPNIA, Service d'Astrophysique, 91191 Gif-sur-Yvette, France.

[6] Laboratoire d'Astrophysique de Marseille, UMR 6110 CNRS–Université de Provence, Traverse du Siphon, BP 8, 13012 Marseille, France.

[7] INAF–Osservatorio di Bologna, via Ranzani 1, 40127 Bologna, Italy.

[8] Institut d'Astrophysique et de Géophysique, Université de Liège, Allée du 6 Août 17, 4000 Liège 1, Belgium.

[9] Dipartimento di Astronomia, Università di Padova, Vicolo dell'Osservatorio 2, I-35122, Padova, Italy.

[10] *Spitzer* Science Center, California Institute of Technology, 100-22, Pasadena, CA 91125.

[11] Astrophysics Group, Blackett Laboratory, Imperial College, Prince Consort Road, London, SW7 2BW, UK.

detected in another because of the unmatched depths of the observations at different wavelengths. The SEDs are also important for evolutionary models (Treister et al. 2004; Silva et al. 2004; Xu et al. 2003; Ballantyne et al. 2006) and to estimate the contribution of accretion to the cosmic backgrounds.

In this work, we characterize the SEDs of a sample of AGNs selected in the hard X-rays and investigate how they vary as a function of X-ray absorption, luminosity, redshift, and host-galaxy contribution. A selection in the hard X-rays minimizes the bias against absorbed AGNs compared to samples selected at soft or broadband X-ray energies. Our analysis is based on the sources detected by *XMM-Newton* in a 1 deg^2 region of the *XMM-Newton* Medium Deep Survey (XMDS; Chiappetti et al. 2005, hereafter Paper I) in the *XMM-Newton* Large-Scale Structure (XMM-LSS) survey field (Pierre et al. 2004, 2007). This region has also been observed as part of the *Spitzer* Wide-Area Infrared Extragalactic survey (SWIRE; Lonsdale et al. 2003) legacy program, of the VIMOS VLT Deep Survey (VVDS; McCracken et al. 2003; Le Fèvre et al. 2004), and of the Canada-France-Hawaii Telescope Legacy "Deep" (D1) Survey. The available multiwavelength data set, the source catalog, and the X-ray observations and data are summarized in § 2 and described in detail in a companion paper (Tajer et al. 2007, hereafter Paper II). Here we present the technique used to classify the SEDs and to estimate photometric redshifts (§ 3). We divide the sample into three main AGN classes based on their SEDs: AGN1, AGN2, and star-forming-galaxy–like AGNs (SF). The average properties of the SEDs of the three AGN classes are described in § 4. Luminosities and absorption are estimated and their role in shaping the observed SEDs are discussed in § 5. The relationship between the X-ray and the mid-IR luminosities is investigated in § 6, and the variations of the mid-IR/X-ray luminosity ratio as a function of X-ray luminosity and AGN class are discussed in § 6. The average SEDs of the three classes regrouped by X-ray luminosity are discussed in § 7. The analysis of the AGN IR colors compared with their luminosity, redshift, and SED classification is presented in § 8. For a subset of sources, radio data are also available. The known radio-IR and radio–X-ray correlations for AGNs and normal galaxies are compared with our data in § 9. Our results are discussed in § 10 and summarized in § 11.

Throughout the paper, we adopt a flat cosmology with $H_0 = 71$ km s^{-1} Mpc^{-1}, $\Omega_M = 0.27$, and $\Omega_\Lambda = 0.73$ (Spergel et al. 2003). For brevity, we refer to the sources in the sample by their XMDS sequence number (XMDS seq.). The names of the sources, complying with the IAU standard, along with the associated identifiers, are reported in Table 1. We use the terms "red" and "blue" to describe the broadband SED shape, where "red" and "blue" mean, respectively, increasing and decreasing fluxes, in νF_ν, at longer wavelengths. Fluxes refer to observed values, not absorption- or k-corrected values, unless specified otherwise. The term "absorbed" refers to X-ray sources with effective column densities $N_H \geq 10^{22}$ cm^{-2} and "obscured" to sources with red optical and IR spectra, implying dust extinction. The X-ray luminosity refers to the rest-frame broadband (0.5–10 keV) luminosity corrected for intrinsic absorption, unless specified otherwise. We use the terms "type 1" and "type 2" for AGNs with broad and narrow optical emission lines, respectively, in their optical spectra. We introduce a new nomenclature for the broadband SED classification: AGN1, AGN2, and SF. The term "AGN1" refers to an SED that is fitted by a type 1 AGN template, the term "AGN2" refers to an SED that is fitted by a type 2 AGN or composite template, and the term "SF," which stands for "star-forming," refers to an SED that is fitted by a star-forming galaxy template, such as spiral and starburst galaxies. Although

the templates are classified on the basis of their optical spectral properties, we do not expect a perfect match between the SED classification and the properties of the optical spectra. The SED classification is more indicative of the main emitting components dominating at optical and IR wavelengths rather than of their optical spectra. Moreover, optical spectra can be affected by host-galaxy dilution (Moran et al. 2002), obscuration (Barger et al. 2001; Rigby et al. 2006), and instrumental and observational limitations, e.g., the lack of emission lines for sources in certain redshift ranges.

2. SAMPLE AND MULTIWAVELENGTH DATA SET

The sample studied in this work includes 136 sources detected at $\geq 3\,\sigma$ in the 2–10 keV X-ray band, corresponding to $\simeq 10^{-14}$ erg cm^{-2} s^{-1}, in a 1 deg^2 region of the XMDS. The XMDS consists of 19 *XMM-Newton* pointings of 20 ks nominal exposure covering a contiguous area of about 2.6 deg^2. The XMDS is complete to a 2–10 keV flux of 9×10^{-14} erg cm^{-2} s^{-1} (Paper I). The 1 deg^2 area chosen for this study is centered at $\alpha_{2000.0} = 2^h26^m$, $\delta_{2000.0} = -4°30'$ (see Paper II for the layout of the selected field on the entire XMDS area) and benefits from a wealth of observations from various surveys: *XMM-Newton* data from the XMM-LSS survey (Pierre et al. 2004, 2007), optical multiband broad photometric data from the VIMOS VLT Deep Survey (VVDS; McCracken et al. 2003; Le Fèvre et al. 2004) and from the Canada-France-Hawaii Telescope Legacy "Wide" (W1) and "Deep" (D1) Surveys (CFHTLS),[12] near-infrared broadband photometric data from the UKIRT Infrared Deep Sky Survey (UKIDSS; Dye et al. 2006; Lawrence et al. 2006), infrared data from the *Spitzer* Wide-Area Infrared Extragalactic survey (SWIRE; Lonsdale et al. 2003), and radio data from the VLA VIRMOS Survey (Bondi et al. 2003; Ciliegi et al. 2005). Optical spectroscopic data are also available from the VVDS for a small subsample (Le Fèvre et al. 2005; Gavignaud et al. 2006), from observations of a selected sample of infrared-selected AGNs (Lacy et al. 2007), and from the 2dF survey (Garcet et al. 2007).

The X-ray observations and data are described in Paper I, and the multiwavelength catalog and data set are presented in Paper II. The X-ray data cover the energy range from 0.3 to 10 keV, and fluxes are measured in five different bands, 0.3–0.5, 0.5–2, 2–4.5, 4.5–10, and 2–10 keV. Column densities are estimated from the hardness ratio derived from the soft (0.5–2 keV) and hard (2–10 keV) counts. For 55 sources with more than 50 net counts, the column density is estimated through spectral modeling with XSPEC (Arnaud 1996; for more details see Paper II).

The VVDS data set includes broadband photometric data in the B, V, R, and I filters, to an AB limiting magnitude (50% completeness for point sources) of 26.5, 26.2, 25.9, and 25.0, respectively (McCracken et al. 2003). Imaging data in the U band to an AB limiting magnitude of $\sim$25.4 are also available. The CFHTLS data set includes broadband photometric data in the u^*, g', r', i', and z filters, to an AB limiting magnitude (50% completeness) of $i' = 24.5$ in the wide survey and $i' = 26.1$ in the deep survey.

Near-infrared data in the J and K bands are available for a small fraction ($\sim$4%) of the area down to an AB limiting magnitude (50% completeness) of 24.2 and 23.9, respectively. Additional near-infrared data from the UKIDSS project are also available. The UKIDSS observations cover about 54% of the XMDS area and include J- and K-band data to a limiting magnitude of 22.3 and 20.8, respectively.

The *Spitzer* infrared data include broadband photometric data from the four IRAC bands at 3.6, 4.5, 5.8, and 8.0 μm to a 5 σ

---

[12] See http://www.cfht.hawaii.edu/Science/CFHTLS/.

TABLE 1

Luminosities, Photometric z, and Classification of the Hard X-Ray Selected Sample

XMDS Seq. (1)	Source Name (2)	z_{phot} (3)	z_{spec} (4)	Sp. Type (5)	N_H^{eff} (10^{22} cm^{-2}) (6)	L_{BX} (erg s^{-1}) (7)	L_{BX}^{corr} (erg s^{-1}) (8)	L_{HX}^{corr} (erg s^{-1}) (9)	$L_{1.4\ GHz}$ (erg s^{-1} Hz^{-1}) (10)	L_{mid-IR} ($L_\odot$) (11)	A_V (12)	SED Type (13)	SED Class (14)	Comment (15)
4..........	XMDS J022521.0−043949	0.245	0.265[a]	2	0.757	43.29	43.42	43.22	<29.21	43.57	0.40	Sb	SF	
12..........	XMDS J022544.9−043735	3.597	3.589[b]	1	29.825	45.54	45.67	45.42	<31.86	46.31	0.55	TQSO1	AGN1	
13..........	XMDS J022504.5−043707	1.103	...	...	3.287	44.32	44.45	44.20	<30.66	45.08	0.05	Mrk231	AGN2	
16..........	XMDSJ022506.4−043621	0.850	...	...	<0.129	43.97	43.97	43.68	<30.39	44.46	0.20	Sey18	AGN2	
18..........	XMDS J022510.6−043549	1.612	...	...	1.917	44.89	44.94	44.71	31.07	45.42	0.10	I19254	AGN2	
29..........	XMDS J022521.0−043228	0.868	...	...	2.663	43.79	43.93	43.68	<30.42	44.41	0.10	Arp220	SF	
36..........	XMDS J022449.8−043026	1.043	...	...	1.773	44.44	44.53	44.32	<30.61	45.12	0.50	BQSO1	AGN1	
40..........	XMDS J022510.6−042928	1.955	...	...	27.436	44.92	45.14	44.91	<31.25	45.73	0.40	Mrk231	AGN2	
55..........	XMDS J022522.8−042648	1.135	1.029[a]	2	4.359	44.21	44.37	44.19	31.00	45.14	0.25	QSO2	AGN2	
58..........	XMDS J022436.2−042511	0.645	...	...	1.760	43.74	43.88	43.63	30.30	44.21	0.10	Mrk231	AGN2	
60..........	XMDS J022439.6−042401	0.203	0.478[a]	2	<0.072	43.81	43.81	43.61	30.08	44.59	0.00	QSO2	AGN2	
67..........	XMDS J022537.0−042132	0.961	...	...	<0.150	44.38	44.37	44.05	<30.52	45.18	0.15	BQSO1	AGN1	
71..........	XMDS J022511.9−041911	1.401	...	...	8.182	44.78	44.95	44.72	<30.91	45.54	0.55	Mrk231	AGN2	
91..........	XMDS J022710.0−041649	1.005	...	...	<0.159	44.25	44.25	44.07	<30.57	44.27	0.30	Sey18	AGN2	B
		0.396	...	...	<0.062	43.26	43.27	43.09	<29.61	43.64	0.15	spi1_4	SF	B
94..........	XMDS J022643.8−041626	0.349	...	...	1.229	43.44	43.70	43.46	<29.48	44.34	0.00	QSO2	AGN2	
101..........	XMDS J022809.4−041524	0.874	...	...	<0.134	44.24	44.24	44.03	...	43.69	0.00	Sb	SF	No IR
106..........	XMDS J022719.5−041407	0.387	...	...	10.289	42.73	43.09	42.83	30.20	44.11	0.55	I22491	AGN2	
111..........	XMDS J022735.6−041317	2.015	...	...	5.069	45.08	45.17	45.00	31.71	45.68	0.00	I19254	AGN2	B, No IR
		2.514	...	...	7.548	45.32	45.40	45.23	31.93	44.40	0.00	Sc	SF	B, No IR
112..........	XMDS J022809.0−041232	0.900	0.878[a]	1	0.386	45.08	45.12	44.87	...	45.86	0.55	TQSO1	AGN1	No IR
114..........	XMDS J022649.7−041240	0.375	...	...	<0.060	43.22	43.22	42.99	29.60	43.73	0.15	Sc	SF	
118..........	XMDS J022649.3−041154	1.195	1.157[b]	1	<0.193	44.38	44.37	44.05	<30.71	44.55	0.20	Sey18	AGN2	
120..........	XMDS J022735.7−041122	1.167	...	...	0.732	45.05	45.09	44.84	31.12	44.17	0.00	Sey2	AGN2	B, No IR
		1.078	...	...	0.656	44.96	45.00	44.76	31.03	44.61	0.15	Sey18	AGN2	B, No IR
124..........	XMDS J022659.7−041108	0.371	...	...	6.730	43.09	43.40	43.14	<29.54	43.92	0.10	QSO2	AGN2	
133..........	XMDS J022713.1−040912	0.723	...	...	1.200	43.91	44.00	43.74	<30.23	43.86	0.10	QSO2	AGN2	M
134..........	XMDS J022701.3−040912	0.755	...	...	<0.113	43.74	43.74	43.52	<30.27	44.48	0.00	Sey18	AGN2	
138..........	XMDS J022656.0−040821	0.546	...	...	7.348	43.17	43.45	43.20	<29.94	44.19	0.00	Sey2	AGN2	
139..........	XMDS J022727.7−040806	0.729	...	...	<0.108	44.02	44.02	43.74	<30.23	44.50	0.00	Sey18	AGN2	Bu, No IR
140..........	XMDS J022701.3−040751	0.235	0.220[a]	2	0.101	43.01	43.05	42.86	<29.03	43.53	0.25	Sd	SF	
142..........	XMDS J022644.1−040720	0.573	...	...	<0.085	43.81	43.81	43.53	30.01	44.62	0.50	BQSO1	AGN1	
143..........	XMDS J022655.4−040650	0.374	...	...	2.817	42.98	43.20	42.95	29.59	43.89	0.35	QSO2	AGN2	
144..........	XMDS J022652.0−040556	0.864	...	...	<0.132	44.28	44.28	44.09	<30.41	44.59	0.00	Sey18	AGN2	
149..........	XMDS J022707.2−040438	0.493	...	...	0.169	43.47	43.50	43.26	<29.83	44.31	0.55	Sey18	AGN2	
161..........	XMDS J022700.7−042020	0.086	0.053[c]	1	<0.030	42.83	42.84	42.44	27.95	43.51	0.00	QSO2	AGN2	
178..........	XMDS J022544.6−041936	0.059	...	...	0.223	41.82	41.90	41.66	<27.81	42.07	0.10	S0	SF	
179..........	XMDS J022607.7−041843	0.328	0.495[a]	1	<0.074	44.29	44.29	44.05	<29.84	44.68	0.45	BQSO1	AGN1	
191..........	XMDS J022626.5−041214	0.779	...	...	19.818	44.11	44.44	44.18	<30.30	44.98	0.55	QSO2	AGN2	
197..........	XMDS J022539.0−040823	0.824	...	...	9.338	44.02	44.27	44.02	<30.36	44.76	0.55	Sey18	AGN2	
199..........	XMDS J022614.5−040738	2.411	...	...	37.558	45.15	45.36	45.12	<31.47	45.35	0.00	QSO2	AGN2	Bu, M
227..........	XMDS J022511.4−041916	1.446	...	...	11.553	44.74	44.94	44.69	<30.95	44.59	0.20	N6090	SF	B
		1.683	...	...	14.693	44.91	45.10	44.85	<31.10	44.79	0.50	TQSO1	AGN1	B
229..........	XMDS J022406.4−041830	1.128	...	...	54.869	44.27	44.69	44.43	<30.69	44.54	0.05	N6090	SF	
232..........	XMDS J022449.2−041800	0.581	...	...	<0.086	43.75	43.75	43.46	<30.00	44.01	0.00	Sey18	AGN2	
233..........	XMDS J022456.0−041725	1.293	...	...	1.114	44.45	44.50	44.25	<30.83	44.83	0.55	TQSO1	AGN1	Bu

TABLE 1—*Continued*

XMDS Seq. (1)	Source Name (2)	$z_{\rm phot}$ (3)	$z_{\rm spec}$ (4)	Sp. Type (5)	$N_{\rm H}^{\rm eff}$ (10^{22} cm^{-2}) (6)	$L_{\rm BX}$ (erg s^{-1}) (7)	$L_{\rm BX}^{\rm corr}$ (erg s^{-1}) (8)	$L_{\rm HX}^{\rm corr}$ (erg s^{-1}) (9)	$L_{\rm 1.4\,GHz}$ (erg s^{-1} Hz^{-1}) (10)	$L_{\rm mid\text{-}IR}$ ($L_\odot$) (11)	A_V (12)	SED Type (13)	SED Class (14)	Comment (15)
242	XMDS J022437.8−041520	1.051	...	...	5.200	44.07	44.24	43.99	<30.61	44.14	0.55	spi1_4	SF	
246	XMDS J022415.6−041416	2.106	...	...	2.382	45.18	45.22	44.97	<31.33	45.84	0.50	QSO1	AGN1	
253	XMDS J022451.9−041209	1.686	...	...	<0.341	44.79	44.78	44.55	31.35	46.08	0.15	TQSO1	AGN1	
255	XMDS J022408.4−041149	1.929	...	...	30.718	44.70	44.94	44.69	31.26	45.10	0.05	Arp220	SF	B
	...	0.357	...	...	4.156	42.90	43.15	42.91	<29.50	43.16	0.10	Sd	SF	B
258	XMDS J022447.4−041049	2.628	...	...	21.429	45.08	45.23	44.98	<31.55	45.55	0.00	QSO1	AGN1	
270	XMDS J022449.2−040841	0.958	...	...	2.446	43.91	44.03	43.78	<30.52	44.27	0.00	Sey18	AGN2	
271	XMDS J022509.5−040836	2.042	...	...	<0.471	44.99	44.98	44.74	<31.30	45.84	0.40	BQSO1	AGN1	
272	XMDS J022501.6−040752	0.797	...	...	<0.120	44.10	44.11	43.89	<30.33	44.98	0.25	BQSO1	AGN1	
279	XMDS J022421.3−040607	0.260	...	...	1.172	42.77	42.94	42.69	<29.19	44.00	0.35	QSO2	AGN2	
280	XMDS J022417.9−040606	1.633	...	...	16.445	44.59	44.80	44.55	<31.07	44.65	0.20	TQSO1	AGN1	
281	XMDS J022503.2−040538	0.930	...	...	0.061	44.61	44.61	44.36	<30.49	44.57	0.00	Sey18	AGN2	
282	XMDS J022452.1−040518	0.189	...	...	<0.041	42.95	42.96	42.66	<28.88	43.69	0.20	QSO1	AGN1	
288	XMDS J022421.2−040351	0.566	...	...	1.298	43.61	43.73	43.48	<29.97	43.36	0.35	spi2a_12	SF	
291	XMDS J022452.0−040258	0.269	...	...	54.378	42.71	43.40	43.14	29.69	43.90	0.00	QSO2	AGN2	M
330	XMDS J022333.0−041525	2.271	...	...	71.370	44.73	45.03	44.78	...	45.60	0.00	QSO2	AGN2	
351	XMDS J022356.5−041105	0.927	...	...	0.679	44.06	44.10	43.86	...	44.25	0.00	Sey18	AGN2	
359	XMDS J022325.3−040922	1.154	...	...	17.337	43.93	44.20	43.95	...	44.26	0.00	spi1_4	SF	
403	XMDS J022742.1−043607	3.493	...	...	32.273	45.46	45.60	45.35	32.38	45.39	0.20	N6090	SF	Bu
406	XMDS J022732.7−043544	0.713	...	...	7.860	44.01	44.26	44.02	30.75	44.49	0.55	TQSO1	AGN1	
414	XMDS J022726.3−043327	3.666	...	...	10.703	45.50	45.56	45.31	<31.88	46.34	0.10	BQSO1	AGN1	
416	XMDS J022812.2−043230	1.668	...	...	<0.335	44.94	44.94	44.73	...	45.00	0.05	BQSO1	AGN1	No IR
420	XMDS J022729.2−043225	2.357	2.290[b]	1	<0.577	45.14	45.13	44.89	<31.41	46.20	0.00	QSO1	AGN1	
427	XMDS J022758.6−043112	0.859	...	...	<0.131	43.91	43.91	43.68	<30.40	44.80	0.00	I19254	AGN2	No IR
430	XMDS J022737.1−043031	0.760	...	...	0.537	43.93	43.98	43.74	<30.28	43.90	0.40	Sey18	AGN2	
438	XMDS J022756.3−042905	0.375	...	...	12.691	42.76	43.15	42.89	<29.55	43.58	0.00	Arp220	SF	No IR
439	XMDS J022746.0−042853	1.988	1.368[d]	3	13.195	44.15	44.36	44.12	30.93	44.03	0.20	Sd	SF	
440	XMDS J022748.8−042820	2.574	...	...	0.509	45.43	45.42	45.22	<31.53	46.21	0.00	QSO1	AGN1	No IR
449	XMDS J022815.2−042617	2.504	...	...	21.945	45.03	45.20	44.95	...	44.60	0.40	spi1_4	SF	B, No IR
		2.438	...	...	20.886	45.00	45.17	44.92	...	44.57	0.00	Sey18	AGN2	B, No IR
453	XMDS J022802.3−042546	0.568	...	...	5.450	43.47	43.71	43.48	...	44.35	0.30	QSO2	AGN2	No IR
470	XMDS J022804.5−041818	1.886	...	...	<0.411	45.01	45.00	44.79	...	45.41	0.00	I19254	AGN2	B, No IR
		0.418	...	...	<0.065	43.39	43.40	43.19	...	42.51	0.00	spi1_4	SF	B, No IR, M
		1.082	...	...	<0.176	44.41	44.41	44.20	...	43.88	0.00	I22491	AGN2	B, No IR
487	XMDS J022643.6−043317	0.489	0.308[a]	3	5.507	42.95	43.25	43.00	29.76	44.29	0.20	spi1_4	SF	M
498	XMDS J022629.2−043057	1.903	2.031[a]	1	<0.466	45.41	45.40	45.20	<31.29	45.82	0.00	QSO1	AGN1	
503	XMDS J022649.3−042920	0.723	0.634[d]	3	4.310	43.62	43.83	43.58	<30.09	44.38	0.00	QSO2	AGN2	
505	XMDS J022649.0−042745	0.084	0.327[a]	2	<0.054	43.07	43.08	42.86	<29.42	44.01	0.00	Sey18	AGN2	
521	XMDS J022658.8−042321	1.754	1.325[d]	3	2.550	44.84	44.93	44.74	30.93	44.89	0.05	Sey2	AGN2	
523	XMDS J022622.1−042221	1.586	2.006[b]	1	<0.456	45.40	45.39	45.11	<31.28	45.96	0.00	BQSO1	AGN1	
551	XMDS J022342.0−043533	1.128	...	...	1.723	44.44	44.52	44.28	...	45.12	0.35	QSO1	AGN1	
561	XMDS J022424.1−043228	1.678	...	...	<0.338	45.05	45.05	44.72	<31.10	45.79	0.00	BQSO1	AGN1	
564	XMDS J022350.7−043157	0.224	...	...	<0.044	42.71	42.72	42.51	...	43.57	0.00	Sey18	AGN2	
565	XMDS J022356.8−043115	1.051	...	...	0.774	44.26	44.31	44.06	...	43.98	0.55	spi1_4	SF	
567	XMDS J022432.4−043036	0.588	...	...	<0.087	43.85	43.86	43.59	<30.01	44.21	0.10	BQSO1	AGN1	
571	XMDS J022330.2−043004	2.404	2.666[a]	1	5.506	45.40	45.45	45.21	...	46.31	0.40	QSO1	AGN1	
577	XMDS J022438.9−042705	0.188	0.252[c]	2	<0.047	43.69	43.70	43.39	29.51	44.31	0.10	Sey18	AGN2	

TABLE 1—*Continued*

XMDS Seq. (1)	Source Name (2)	$z_{\rm phot}$ (3)	$z_{\rm spec}$ (4)	Sp. Type (5)	$N_{\rm H}^{\rm eff}$ (10^{22} cm^{-2}) (6)	$L_{\rm BX}$ (erg s^{-1}) (7)	$L_{\rm BX}^{\rm corr}$ (erg s^{-1}) (8)	$L_{\rm HX}^{\rm corr}$ (erg s^{-1}) (9)	$L_{\rm 1.4\,GHz}$ (erg s^{-1} Hz^{-1}) (10)	$L_{\rm mid\text{-}IR}$ ($L_\odot$) (11)	A_V (12)	SED Type (13)	SED Class (14)	Comment (15)
578..........................	XMDS J022350.7−042703	1.033	...	...	<0.165	44.22	44.22	43.88	...	44.69	0.25	QSO1	AGN1	
602..........................	XMDS J022351.2−042054	0.097	0.181[a]	2	2.836	42.41	42.67	42.42	...	43.64	0.00	M82	SF	
626..........................	XMDS J022326.0−043534	1.149	...	...	1.191	44.63	44.69	44.45	...	44.91	0.00	N6090	SF	
708..........................	XMDS J022605.3−045803	1.476	...	...	<0.276	44.75	44.75	44.50	<30.97	44.77	0.00	Sey18	AGN2	
709..........................	XMDS J022606.7−045722	0.661	...	...	<0.098	43.91	43.91	43.60	<30.13	44.26	0.00	Sey18	AGN2	
710..........................	XMDS J022627.4−045710	2.320	...	...	0.931	45.55	45.56	45.35	32.11	45.97	0.50	TQSO1	AGN1	
718..........................	XMDS J022615.1−045355	0.896	...	...	0.900	44.08	44.14	43.94	30.64	44.23	0.45	spi1_4	SF	
720..........................	XMDS J022628.9−045252	2.027	...	...	<0.465	45.14	45.13	44.88	<31.29	45.40	0.50	BQSO1	AGN1	
731..........................	XMDS J022554.1−044921	0.534	...	...	2.107	43.26	43.42	43.17	<29.91	43.93	0.55	QSO2	AGN2	
738..........................	XMDS J022556.1−044724	0.898	1.010[a]	1	<0.160	44.49	44.49	44.25	31.92	44.66	0.00	Sey18	AGN2	
739..........................	XMDS J022617.1−044724	0.184	0.140[a]	2	2.820	42.11	42.38	42.14	29.32	43.56	0.05	spi1_4	SF	M
742..........................	XMDS J022514.3−044659	1.615	1.924[a]	1	<0.425	45.29	45.28	45.04	31.34	46.23	0.10	BQSO1	AGN1	
743..........................	XMDS J022625.2−044647	1.556	...	...	2.256	44.74	44.80	44.56	<31.02	45.25	0.15	Mrk231	AGN2	
746..........................	XMDS J022512.6−044633	0.219	...	...	5.213	43.04	43.36	43.10	<29.02	43.02	0.55	Sb	SF	
747..........................	XMDS J022640.4−044606	1.248	...	...	23.531	44.49	44.79	44.53	31.61	45.17	0.00	I19254	AGN2	B
		1.248	...	...	23.531	44.49	44.79	44.53	31.61	45.17	0.00	I19254	AGN2	B
748..........................	XMDS J022610.9−044550	2.886	...	...	12.547	45.32	45.42	45.17	<31.65	45.79	0.40	TQSO1	AGN1	
755..........................	XMDS J022600.1−044412	0.730	...	...	<0.108	44.06	44.06	43.83	<30.24	44.59	0.10	Mrk231	AGN2	
760..........................	XMDS J022531.4−044210	0.833	1.228[d]	3	150.000[e]	45.31	46.21	45.96	<30.78	44.41	0.40	Sey18	AGN2	
779..........................	XMDS J022321.8−045740	0.637	...	...	16.471	43.93	44.28	44.02	...	45.26	0.00	Mrk231	AGN2	
780..........................	XMDS J022332.0−045740	0.963	...	...	<0.151	44.31	44.31	44.07	...	45.04	0.00	Sey18	AGN2	
782..........................	XMDS J022326.3−045708	0.839	0.826[a]	1	<0.125	44.12	44.12	43.98	...	44.72	0.00	Sey18	AGN2	
787..........................	XMDS J022317.9−045527	0.981	...	...	9.800	43.91	44.14	43.90	...	43.69	0.15	Sey18	AGN2	
788..........................	XMDS J022353.7−045510	0.958	...	...	0.085	44.58	44.58	44.36	...	44.68	0.40	QSO1	AGN1	
789..........................	XMDS J022329.1−045452	0.646	0.604[a]	1	<0.089	43.84	43.84	43.56	...	44.44	0.00	Sey18	AGN2	
800..........................	XMDS J022403.8−045120	0.874	...	...	<0.134	44.13	44.13	43.88	<30.42	44.66	0.55	Sey18	AGN2	
801..........................	XMDS J022344.4−045120	0.959	...	...	1.167	44.09	44.16	43.92	...	44.24	0.00	Sey18	AGN2	
807..........................	XMDS J022333.0−044924	2.039	2.302[a]	1	2.460	45.08	45.12	44.87	...	45.53	0.00	BQSO1	AGN1	
817..........................	XMDS J022354.5−044815	2.428	2.458[a]	1	<0.657	45.23	45.21	44.91	...	46.67	0.00	QSO1	AGN1	
820..........................	XMDS J022319.4−044732	0.640	0.293[a]	2	0.185	43.18	43.23	43.03	...	44.27	0.00	QSO2	AGN2	
825..........................	XMDS J022330.6−044633	1.735	...	...	3.157	45.05	45.12	44.84	...	45.34	0.10	Mrk231	AGN2	
828..........................	XMDS J022318.8−044616	0.673	...	...	<0.100	43.75	43.75	43.53	...	44.28	0.05	QSO1	AGN1	
840..........................	XMDS J022330.9−044235	2.297	...	...	13.666	45.05	45.19	44.94	...	45.39	0.55	Mrk231	AGN2	Bu
842..........................	XMDS J022402.4−044140	0.010	0.0433[f]	3	1.761	41.26	41.49	41.24	29.28	43.71	0.30	Sd	SF	
844..........................	XMDS J022343.2−044105	1.493	...	...	60.833	44.46	44.83	44.57	...	45.36	0.05	I19254	AGN2	B
		1.857	...	...	86.702	44.69	45.07	44.81	...	45.32	0.25	I22491	AGN2	B
846..........................	XMDS J022317.2−044035	0.765	0.842[a]	1	<0.128	44.27	44.27	44.11	...	45.61	0.45	BQSO1	AGN1	
1197..........................	XMDS J022720.2−045738	1.116	...	...	15.507	44.16	44.42	44.18	<30.68	44.95	0.25	I22491	AGN2	
1199..........................	XMDS J022651.6−045714	0.290	0.331[a]	2	0.249	43.54	43.60	43.37	<29.43	43.85	0.00	QSO2	AGN2	
1201..........................	XMDS J022723.4−045608	0.168	...	...	0.295	42.28	42.36	42.12	<28.77	42.39	0.00	Sey18	AGN2	
1219..........................	XMDS J022701.6−045158	2.112	...	...	25.148	44.66	44.86	44.62	32.45	45.13	0.55	M82	SF	Bu
1226..........................	XMDS J022711.7−045038	0.946	...	...	0.215	44.81	44.82	44.59	<30.50	44.93	0.55	BQSO1	AGN1	
1227..........................	XMDS J022736.8−045033	0.445	...	...	1.147	43.32	43.45	43.26	29.91	44.19	0.00	Sey2	AGN2	

TABLE 1—*Continued*

XMDS Seq. (1)	Source Name (2)	z_{phot} (3)	z_{spec} (4)	Sp. Type (5)	N_H^{eff} (10^{22} cm^{-2}) (6)	L_{BX} (erg s^{-1}) (7)	L_{BX}^{corr} (erg s^{-1}) (8)	L_{HX}^{corr} (erg s^{-1}) (9)	$L_{1.4\,GHz}$ (erg s^{-1} Hz^{-1}) (10)	$L_{mid\text{-}IR}$ ($L_\odot$) (11)	A_V (12)	SED Type (13)	SED Class (14)	Comment (15)
1231............	XMDS J022731.9−044957	0.741	. . .	. . .	<0.110	43.62	43.62	43.39	30.85	44.18	0.30	Sey18	AGN2	
1236............	XMDS J022729.0−044857	1.513	. . .	. . .	14.984	44.31	44.52	44.28	<30.99	45.51	0.40	I19254	AGN2	
1246............	XMDS J022712.8−044636	1.446	. . .	. . .	<0.267	44.74	44.74	44.48	32.85	46.02	0.00	BQSO1	AGN1	
1247............	XMDS J022633.1−044637	1.197	. . .	. . .	3.040	44.56	44.68	44.42	<30.75	44.91	0.00	QSO2	AGN2	
1248............	XMDS J022725.4−044619	0.034	. . .	. . .	<0.029	41.30	41.32	41.09	<27.31	42.60	0.00	Sa	SF	M
1252............	XMDS J022716.0−044539	0.590	. . .	. . .	<0.087	44.07	44.08	43.82	<30.02	44.55	0.50	BQSO1	AGN1	
1264............	XMDS J022751.3−044251	1.694	. . .	. . .	<0.343	44.95	44.94	44.79	<31.11	45.42	0.10	BQSO1	AGN1	
1265............	XMDS J022712.6−044221	0.232	0.205[a]	2	2.526	42.94	43.18	42.93	29.48	43.95	0.55	spi1_4	SF	

NOTES.—Col. (1): X-ray catalog sequence number (Paper I; Paper II). Col. (2): IAU official source name. Col. (3): Photometric redshift. Col. (4): Spectroscopic redshift. Col. (5): Spectroscopic classification (1, type 1 AGN; 2, type 2 AGN; 3, star-forming galaxy). Col. (6): Effective column density (Paper II). Upper limits are derived from the minimum value of 2.6×10^{20} cm^{-2} corresponding to the Galactic value, when no additional absorption was required. Col. (7): Logarithm of the rest-frame broadband (0.5–10 keV) luminosity not corrected for absorption. Col. (8): Logarithm of the absorption-corrected rest-frame broadband (0.5–10 keV) luminosity. Col. (9): Logarithm of the absorption-corrected rest-frame hard-band (2–10 keV) luminosity. All X-ray luminosities have been derived assuming an absorbed power-law spectrum with photon index $\Gamma = 1.7$ and column density N_H^{eff}. Broadband X-ray luminosities have been derived from the broadband fluxes, and hard-band X-ray luminosities have been derived from the hard-band fluxes (see Paper II). Col. (10): Logarithm of the monochromatic radio luminosity at 1.4 GHz rest frame. Col. (11): Logarithm of the integrated mid-IR luminosity in the 3–20 μm rest-frame wavelength range. Col. (12): Optical extinction derived from the best fit assuming the prescription reported in Calzetti et al. (2000). Col. (13): Best-fit template (see Fig. 1). Col. (14): AGN spectral classification (SF, AGN1, AGN2). Col. (15): Comments. "B" indicates a source in sample B, "Bu" marks those in sample B with unreliable poorly sampled SED, "M" refers to a source for which the absolute magnitude criterion for the photometric redshift determination was relaxed, and "No IR" indicates sources without SWIRE coverage.

[a] Spectroscopic redshift from Garcet et al. (2007).
[b] Spectroscopic redshift from Gavignaud et al. (2006).
[c] Spectroscopic redshift from Lacy et al. (2007).
[d] Spectroscopic redshift from Le Fèvre et al. (2005).
[e] Fixed maximum value of the intrinsic column density.
[f] Spectroscopic redshift from NED.

limit of 4.3, 8.3, 58.5, and 65.7 μJy, respectively, and MIPS data at 24 μm to a 5 σ limit of 241 μJy. The SWIRE observations cover about 90% of the area and are available for 122 sources, 91% of the entire sample.

The radio data are from the VLA VIRMOS Survey, which reaches a 5 σ depth of 80 μJy at 1.4 GHz (Bondi et al. 2003; Ciliegi et al. 2005).

The associations between the X-ray source list and the multi-wavelength catalogs are described in detail in Paper I and Paper II. The selected multiwavelength catalog contains 136 sources. Two sources are galaxy clusters (see Paper II) and are not included in the following analysis. Of the remaining 134 sources, 130 have optical counterparts, unique for 121 and multiple candidates for the other remaining nine sources. Of four sources without optical counterpart, one is close to a bright star and the photometry could not be extracted, and the remaining three sources are optically blank fields. All of the 122 sources that fall into the SWIRE area are detected in at least two *Spitzer* bands, and 87 are also detected at 24 μm. UKIDSS data are available for 66 sources, of which 55 are also SWIRE sources and 64 have an optical counterpart. Radio data are available for 32 sources, of which 30 are also SWIRE sources and 30 have an optical counterpart.

3. TEMPLATE FITTING AND PHOTOMETRIC REDSHIFT TECHNIQUE

In order to classify the SEDs and estimate photometric redshifts of the sources in the sample, optical and IR data are combined and fitted with a library of galaxy and AGN templates. The SEDs are fitted using the HYPERZ code (Bolzonella et al. 2000). HYPERZ has already successfully been applied to various data sets and offers the possibility of using any template library and filters set. HYPERZ finds the best fit by minimizing the χ^2 derived from the comparison of the observed SED and expected SEDs, at various redshifts, derived from the templates using the same photometric system. The effects of dust extinction are taken into account by reddening the reference templates according to a selected reddening law. We use the prescription for extinction derived from high-redshift starbursts by Calzetti et al. (2000). In order to limit degeneracies in the best-fit solutions we limit the extinction A_V to be less than 0.55 mag and include templates of highly extincted objects to fit heavily obscured sources.

The library contains 20 templates including one elliptical, seven spiral, three starburst, six AGN, and three composite (starburst + AGN) templates covering the wavelength range between 1000 Å and 1000 μm. The elliptical, spiral, and starburst templates were generated with the GRASIL code (Silva et al. 1998). The seven spirals range from early to late types (S0–Sd), and the starburst templates correspond to the SEDs of NGC 6090, M82 and Arp 220. In all of the spiral and starburst templates the spectral region between 5 and 12 μm, where many broad emission and absorption features are observed, was replaced using observed IR spectra from the PHT-S spectrometer on board the *Infrared Space Observatory* (*ISO*) and from the IRS on board *Spitzer*.

Templates of moderately luminous AGNs, representing Seyfert 1.8 and Seyfert 2 galaxies, were obtained by combining models, broadband photometric data (NED), and *ISO* PHT-S spectra (B. Schulz 2003, private communication) of a random sample of 28 Seyfert galaxies. The other four AGN templates include three templates representing optically selected QSOs with different values of IR/optical flux ratios (QSO1, TQSO1, and BQSO1) and one type 2 QSO (QSO2). The QSO1 templates are derived by combining the SDSS quasar composite spectrum and rest-frame IR data of a sample of 35 SDSS/SWIRE quasars (Hatziminaoglou et al. 2005). After normalizing each SED in the optical, we de-
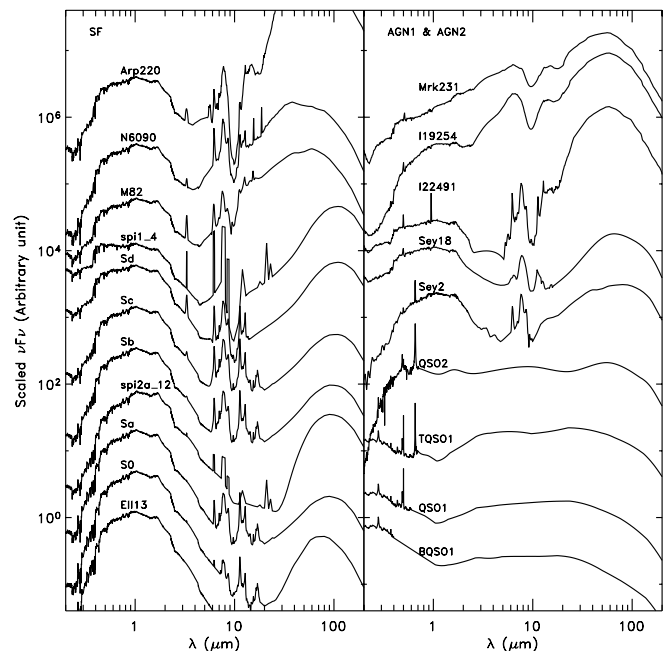
Fig. 1.—SEDs in νF_ν vs. λ of the template library used in this work. *Left:* Elliptical, spiral, and starburst galaxy templates. *Right:* AGN templates; the type 2 AGNs are the top six and the type 1 AGNs are the bottom three. The names of the templates are annotated.

rived three templates with the same optical spectrum but three different IR SEDs. The QSO1 IR template was obtained from the average fluxes of all the measurements regrouped in wavelength bins, the TQSO1 IR template was obtained from the highest 25% measurements per bin, and the BQSO1 IR template was obtained from the lowest 25% measurements per bin. The type 2 QSO template (QSO2) was obtained by combining the observed optical/near-IR spectrum of the red quasar FIRST J013435.7−093102 (Gregg et al. 2002) and the rest-frame IR data from the quasars in the Palomar-Green sample with consistent optical SEDs (Polletta et al. 2006).

The composite (AGN + SB) templates are empirical templates created to fit the SEDs of the following objects: the heavily obscured broad absorption line (BAL) QSO Mrk 231 (Berta 2005), the Seyfert 2 galaxy IRAS 19254−7245 South (I19254; Berta et al. 2003), and the Seyfert 2 galaxy IRAS 22491−1808 (I22491; Berta 2005). All these objects contain a powerful starburst component, mainly responsible for their large infrared luminosities ($>10^{12} L_\odot$), and an AGN component that contributes to the mid-IR luminosities.

The full library of galaxy and AGN templates is shown in Figure 1. With respect to existing template libraries derived from empirical SEDs (Coleman et al. 1980) or from models (Bruzual & Charlot 2003; Fioc & Rocca-Volmerange 1997; Silva et al. 1998; Devriendt et al. 1999), this library has a broader wavelength coverage and variety of spectral types. Examples of application of this library to various types of SWIRE sources can be found in Lonsdale et al. (2004), Franceschini et al. (2005), Hatziminaoglou et al. (2005), Jarrett et al. (2006), Polletta et al. (2006), and Weedman et al. (2006).

Photometric redshift techniques have been applied to optical or optical and near-IR data sets, providing reliable photometric redshifts (Rowan-Robinson et al. 2005; Ilbert et al. 2006; Brodwin et al. 2006). However, with a limited wavelength coverage, some spectral types can be degenerate, e.g., obscured starbursts and ellipticals. In those cases, the inclusion of mid-IR data can break

the degeneracy. However, the inclusion of mid-IR data in photometric redshift techniques can degrade the photometric redshift estimates because the templates represent only a limited range of optical/IR ratios. We compared both approaches, fitting optical + near-IR and optical + near-IR + mid-IR data, and concluded that the latter method gives significantly better results both in the photometric redshift estimates and in spectral type classification.

We fit the SEDs using the data from the optical to 24 μm. Mid-IR (5.8–24 μm) data are available for 107 of the 134 sources in the sample. The best solution corresponds to the solution with minimum χ^2 among all of the solutions with $z = 0–4$ and B-band absolute magnitude within a predefined range. The allowed range of B-band absolute magnitude, M_B, varies with redshift and is different for normal galaxies and for AGN templates; M_B must be greater than $M_B^{\min} = -6 - 5 \log d_L$, where d_L is the luminosity distance in megaparsecs, and lower than $M_B^{\max} = -0.7 - 5 \log d_L$, but always within the range -23.7 to -17 for normal galaxy templates, and greater than $M_B^{\min} = -6.5 - 5 \log d_L$ and lower than $M_B^{\max} = -5 \log d_L$, but always within the range -28.8 to -19 for AGN templates. The best-fit solution is that with the lowest χ^2 among all of the solutions that satisfy the absolute-magnitude criterion. If there are no solutions in the defined absolute magnitude range, the criterion is modified by extending the limits $M_B^{\min}$ and $M_B^{\max}$ by steps of 0.5 mag, but always within the maximum allowed range, -23.7 to -17 for normal galaxy solutions and -28.8 to -19 for AGN solutions. The criterion was relaxed in seven cases (see the M flag in col. [15] of Table 1).

In addition to the best solution, we consider up to two secondary solutions within the defined absolute magnitude limits. In most of the cases there are three solutions per source (the best and two secondary solutions), but in some cases, only one solution (or one minimum in the χ^2 distribution) is found within the defined absolute magnitude limits; thus, for each source there might be from one to three solutions. We refer to these as the acceptable solutions. The comparison between the spectroscopic and final photometric redshifts is shown in Figure 2.

The reliability and accuracy of the photometric redshifts are measured via the fractional error Δz, the systematic mean error $\overline{\Delta z}$, the 1 σ dispersion σ_z, and the rate of catastrophic outliers, defined as the fraction of sources with $|\Delta z| > 0.2$. Δz is defined as

$$\Delta z = \frac{z_{\mathrm{phot}} - z_{\mathrm{spec}}}{1 + z_{\mathrm{spec}}}, \qquad (1)$$

$$\sigma_z^2 = \sum \left(\frac{z_{\mathrm{phot}} - z_{\mathrm{spec}}}{1 + z_{\mathrm{spec}}} \right)^2 \Big/ N, \qquad (2)$$

where N is the number of sources with spectroscopic redshifts. Since there are only 33 sources in the selected sample with a spectroscopic redshift measurement (see Table 1), we also included in the analysis of the photometric redshifts, all of the sources in the XMDS 4 σ VVDS sample (Paper I) with a spectroscopic redshift measurement, for a total of 49 sources. The systematic mean error, $\overline{\Delta z}$, is -0.001 (-0.008), the rms, σ_z, is 0.12 (0.11), and the outlier fraction is 10% (6%) for the 49 sources with spectroscopic redshifts. The values in parentheses correspond to the results obtained using only the 33 sources with spectroscopic redshifts in the hard X-ray selected sample. Although these results are not as satisfactory as those achieved for galaxy populations, even when few broadband photometric data are available (Babbedge et al. 2004), they are better than what has
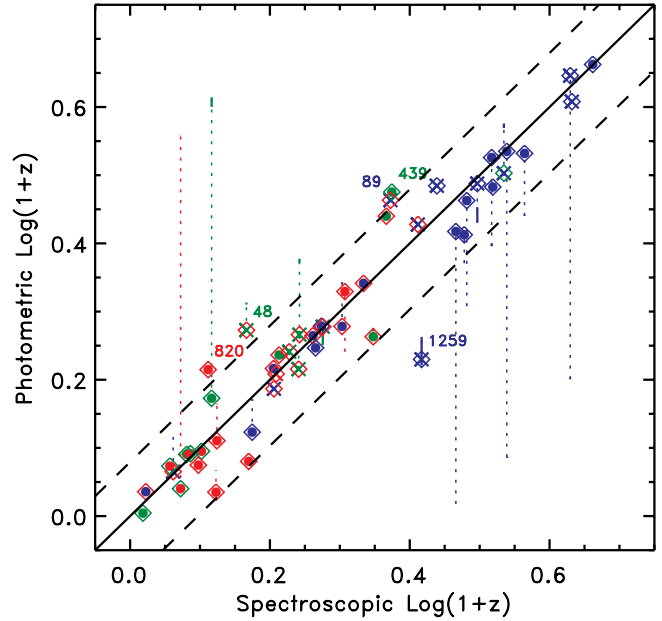
Fig. 2.—Comparison between photometric and spectroscopic redshifts in $\log(1 + z)$ of the 49 sources with available spectroscopic redshifts (*open diamonds*). Dashed lines represent 20% agreement in $1 + z$. The five catastrophic outliers are labeled with their XMDS seq.: 48, 89, 439, 820, and 1259. Filled circles (33 sources) represent the sources in the selected sample presented in this work. Crosses (16 sources) represent the additional sources in the XMDS sample with spectroscopic redshifts. Circles and crosses are color-coded according to the SED class: *blue symbols*, AGN1; *red symbols*, AGN2; *green symbols*, SF. A diamond is overplotted on each source and is color-coded according to the spectroscopic classification: *blue diamond*, type 1 AGN; *red diamond*, type 2 AGN; *green diamond*, normal galaxy. The vertical dotted lines show the range of photometric redshifts of all acceptable solutions (note that the acceptable solutions can be at the extremes of the bar and do not cover a continuous range in redshifts).

been previously obtained for AGN samples. The fraction of outliers for AGNs is indeed usually higher than 25% (Kitsionas et al. 2005; Babbedge et al. 2004). The achieved accuracy does not allow us to perform detailed analysis on single sources. However, it is adequate for a statistical analysis of the population as presented in this work. Four (XMDS seq. 48, 89, 439, and 820) of the five outliers have $|\Delta z| < 0.28$ and two of them (XMDS seq. 439 and 820) are in the hard X-ray sample. The only outlier with $|\Delta z| > 0.28$ is source XMDS seq. 1259, which is not included in the selected sample.

The redshift distribution of the whole sample, based on the photometric redshifts, is shown with a dot-dashed line in Figure 3. The distribution peaks at $z \simeq 0.9$, consistent with the redshift distribution of other X-ray–selected samples (Hasinger 2002; Barger et al. 2002; Szokoly et al. 2004; Eckart et al. 2006). About 54% (73 of 134) of the sources are at redshift below 1 and 90% are at redshift below 2.3. In Figure 3, the redshift distribution of the total sample is compared with that of AGN1, AGN2, and SF sources (see § 3.1).

3.1. Spectral Energy Distributions

According to the template corresponding to the best-fit solution selected by the procedure described above, each source is classified as one of the following broad classes, AGN1, AGN2, or SF. Examples of fits for the three classes are shown in Figure 4. The AGN1 class includes all of the sources best fitted with a QSO1 template (Fig. 1, *bottom three on the right*; see also Fig. 4, *right*). They are characterized by blue optical SEDs ($\lambda F_\lambda \propto \lambda^{-0.9}$ to $\lambda^{-0.4}$) and red IR SEDs ($\lambda F_\lambda \propto \lambda^{0.2}$ and $\propto \lambda^{0.4}$). The change in
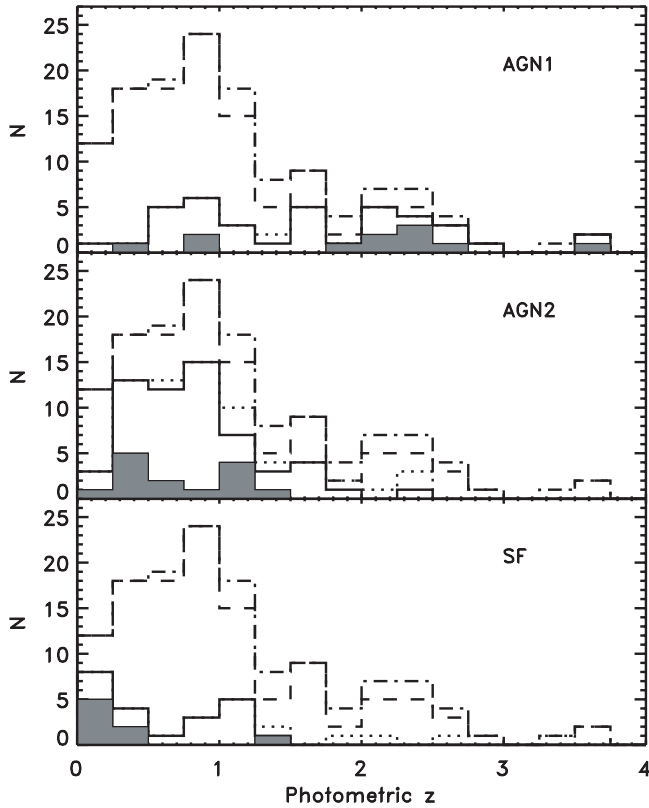
FIG. 3.—Redshift distribution of the entire sample (samples A + B), 134 sources (*dot-dashed line*), and of sample A only, 119 sources (*dashed line*; see § 4). Each panel shows the redshift distributions of the sources classified as AGN1 (*top*), AGN2 (*middle*), and SF (*bottom*). The dotted lines correspond to the sources in each class in the entire sample, and the solid lines only to those in sample A. The shaded area represents the distribution of spectroscopic redshifts in each class.

slope, from blue to red, occurs at about 1 μm. Emission from the accretion disk dominates at shorter wavelengths and from AGN-heated dust at longer wavelength. The AGN2 class includes sources best fitted with the Seyfert templates, the three composite AGN + SB templates, or the QSO2 template (Fig. 1, *top six on the right*; see also Fig. 4, *middle*). The AGN2 templates include a wide variety of SED shapes. They are mostly red at optical and near-IR wavelengths, but in some cases an upturn (blue) at short wavelengths (far-ultraviolet) is present. Their IR SEDs range from red power-law–like SEDs, similar to the AGN1 or redder, to composite SEDs where emission features associated with star formation are present in addition to continuum emission in the near-IR. The SF class includes sources fitted with a spiral or a starburst template (Figs. 1 and 4, *left*). SF templates are all red in the optical and blue in the near-IR, consistent with emission from stellar populations. At mid-IR wavelengths, the SED is dominated by emission features and a warm dust continuum associated with star-forming regions. Photometric and spectroscopic redshifts, best-fit template, and classification are reported in Table 1.

Although a best-fit template, and thus an SED classification, is available for all sources in the sample, in the following analysis we will discuss the results only for sources with a reliable fit and simply report the derived values for the rest of the sample for completeness. We define a fit as reliable if at least six data points could be fitted. Six sources (XMDS seq. 139, 199, 233, 403, 840, and 1219) have been observed only in the optical or in the IR and have fewer than six data points in total. Because of the limited wavelength coverage, they are not included in the following analysis. Nine sources with an ambiguous counterpart (XMDS seq. 91, 111, 120, 227, 255, 449, 470, 747, and 844) are also excluded from the following analysis. We refer to these 15 sources as sample B. In Table 1 we report all best-fit solutions for the sources with an ambiguous counterpart in order of increasing
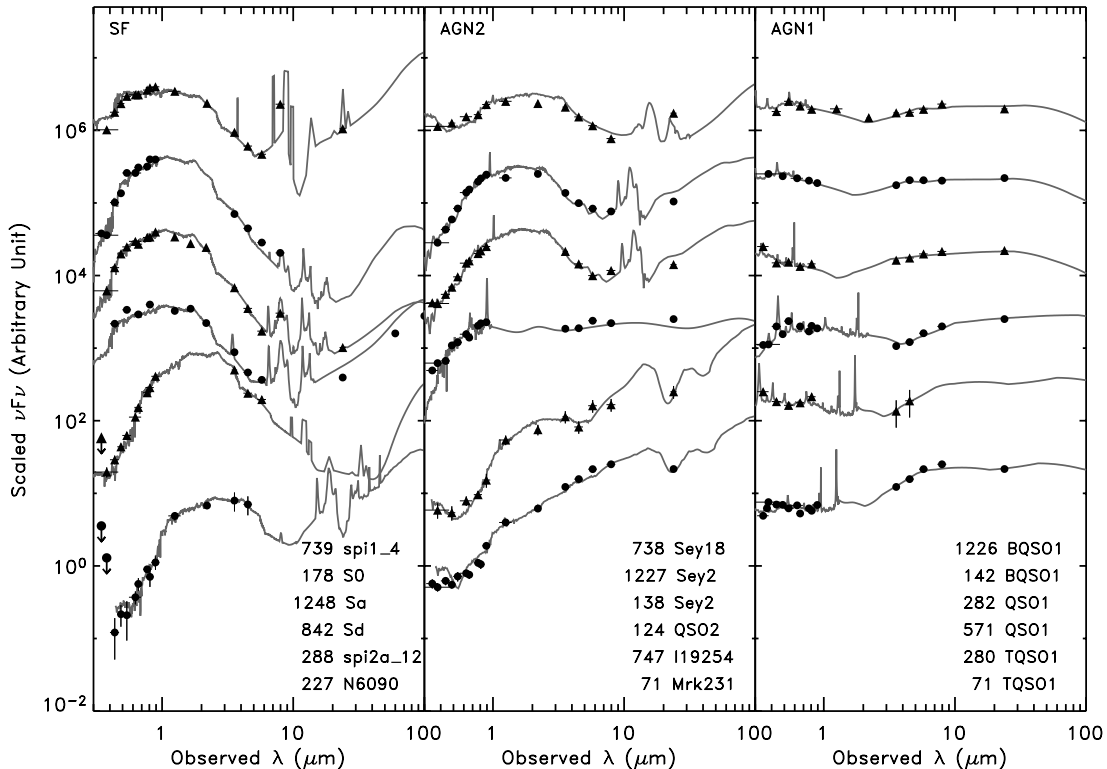
FIG. 4.—Scaled SEDs (*filled circles and triangles*) and best-fit templates (*gray solid curves*) in F_ν vs. λ of 18 sources: six each classified as SF (*left*), AGN2 (*middle*), and AGN1 (*right*). Downward-pointing arrows correspond to 5 σ upper limits. The source sequence number and best-fit template names are listed in the same order as the SEDs are plotted.

distance of the optical counterpart, but in the following figures we will show only the best-fit solution corresponding to the closest counterpart. The sample that will be analyzed in the following sections contains the remaining 119 sources (the total 134 minus the 15 in sample B, hereafter sample A), of which 38 are classified as AGN1s (32% of the sample), 59 (50%) as AGN2s, and the remaining 22 (18%) as SFs.

The reliability of this classification depends on the number of available optical and IR data points and on the ability of identifying the signatures that make the SEDs of the various classes unique. In the case of AGN1s, the blue optical SED and red IR SED provide two clear signatures that make their classification highly reliable (see Fig. 4, *right*). The distinction between AGN2s and SFs is less obvious than the identification of AGN1s since the only difference between their SEDs is in the shape of the near- and mid-IR SED (see Fig. 4, *left and middle*). When only a few IR data points are available or the data do not sample the region where the AGN signature is visible (i.e., 3–5 μm rest frame), the separation between the two classes is more uncertain. In order to estimate the uncertainty of our classification we counted all sources with an acceptable solution in a different class (see § 3 for a description of the acceptable solutions). For each class, we counted the number of sources with solutions in other classes and the number of sources in other classes with a secondary solution in the specific class. For the AGN1 class, we estimate that two sources might belong to a different class, AGN2 or SF, four AGN2s have an AGN1 secondary solution, and two SFs have an AGN1 secondary solution. Thus, there are 36 sources with a secure AGN1 fit and 44 sources with a possible AGN1 fit, which implies an AGN1 fraction of 32^{+5}_{-2}%. Analogously, for the AGN2 class, we estimate that 13 sources might belong to a different class, AGN1 or SF, one AGN1 has an AGN2 solution, and five SFs have an AGN2 solution. Thus, there are 46 sources with a secure AGN2 fit and 65 sources with a possible AGN2 fit, which implies an AGN2 fraction of 50^{+5}_{-11}%. For the SF class, we estimate that seven sources might belong to a different class, AGN1 or AGN2, one AGN1 has an SF solution, and nine AGN2s have an SF solution. Thus, there are 13 sources with a secure SF fit and 30 sources with a possible SF fit, which implies an SF fraction of 18% ± 7%. Note that, by definition, the given uncertainties on the class fractions correspond to lower and upper limits on the fraction of sources in each class.

The reliability and completeness of our classification can be estimated using the spectroscopic classification, but we do not expect an exact correspondence between our SED-based classes and the spectroscopic classes. A spectroscopic classification is available for 49 sources, including sources that are not in the hard X-ray samples. Of these, 26 are spectroscopically classified as type 1 AGNs, 12 as type 2 AGNs, and 11 as star-forming galaxies. Among the 26 type 1 AGNs, 16 are classified AGN1s, 9 as AGN2s, and 1 as an SF, and all the AGN1s with a spectroscopic classification (16) are type 1 AGNs. Thus, the SED classification is 62% complete (16 AGN1s of 26 type 1 AGNs) and 100% reliable (all AGN1s are type 1 AGNs). Among the 12 sources spectroscopically classified as type 2 AGNs, 7 are classified as AGN2s and the remaining as SFs. The AGN2 class (24 sources) includes 9 type 1 AGNs, 7 type 2 AGNs, and 8 SFs. Thus, the completeness of the AGN2 sample is 58% (7 AGN2 of 12 type 2 AGNs), and the reliability is 29% (7 of 24 AGN2s are type 2 AGNs). There are 11 sources with a spectroscopic classification consistent with being normal galaxies; 8 of them are classified as AGN2s and 5 as SF. Among the 9 sources classified as SF, 1 is a type 1 AGN, 5 are type 2 AGNs, and 3 are star-forming galaxies according to the spectroscopic classification. The completeness of the SF sample is

thus 27% (3 of 11 star-forming galaxies are classified SF), and the reliability is 33% (3 of 9 SF sources are star-forming galaxies). In summary, the SED and the spectroscopic classification agree in 26 of the 49 sources with spectroscopic classification (53%).

We can also compare the fraction of AGNs that are identified as AGNs by the SED classification (AGN1 or AGN2) and by the spectroscopic classification (type 1 and type 2 AGNs). Note that all sources are AGNs as probed by their X-ray properties. Of the 49 AGNs with spectroscopic classification, 38 (78%) are spectroscopically identified as AGNs (26 type 1 and 12 type 2), and 40 (82%) are classified AGNs by the SED fitting technique (25 AGN1s and 7 AGN2s). The latter fraction is consistent with the 83% derived from the entire X-ray sample.

3.2. *Redshift-dependent Derived Quantities: Luminosities and Absorption*

Using the available redshifts, spectroscopic if available, photometric otherwise, and the best-fit templates, we derive the luminosities in the broad and hard X-ray energy bands (0.5–10 and 2–10 keV rest frame), in the mid-IR (3–20 μm rest frame), and in the radio at 1.4 GHz rest frame. The X-ray luminosities, hereafter $L_{0.5-10\,\mathrm{keV}}$ and $L_{2-10\,\mathrm{keV}}$, are derived assuming a power-law spectrum $[F(E) \propto E^{-(\Gamma-1)}]$ with photon index $\Gamma = 2.0$. Effective column densities are derived from the observed column densities after applying the redshift correction (see Paper II for details). In case the observed column density is consistent with the Galactic value (2.61×10^{20} cm^{-2}), we derive an upper limit to the effective column by assuming the Galactic value and the redshift of the source (see also § 5). The observed column densities are used to correct the X-ray luminosity for absorption, hereafter $L_{0.5-10\,\mathrm{keV}}^{\mathrm{corr}}$. The uncertainty on the X-ray luminosities are estimated by propagation of the uncertainty on the flux and on the column density.

The mid-IR luminosities, $L_{3-20\,\mu\mathrm{m}}$, are estimated by integrating the best-fit template in the rest-frame 3–20 μm wavelength range. To estimate the uncertainty on the mid-IR luminosities we first fit the IR data ($\lambda_{\mathrm{obs}} > 3.6\,\mu$m) of each source with all of the templates, derive the χ^2, and then use the range of luminosities obtained from all acceptable solutions.

The radio luminosities, $L_{1.4\,\mathrm{GHz}}$, are derived assuming a power-law spectrum ($F_\nu \propto \nu^{-\alpha_R}$) with spectral index $\alpha_R = 0.8$ (Condon & Broderick 1988). The uncertainty on the radio luminosity is derived from the radio flux uncertainty.

The X-ray, mid-IR, and radio luminosities are listed in Table 1.

3.3. *Star-forming Galaxies*

In the following analysis, we will include only sources that contain an AGN. In order to identify sources whose X-ray emission is consistent with emission from a star-forming galaxy, e.g., from X-ray binaries, we require a broad X-ray luminosity below 10^{42} erg s^{-1} and a soft X-ray spectrum. Star-forming galaxies are typically characterized by luminosities below 10^{42} erg s^{-1} and show steep X-ray spectral slopes (Kim et al. 1992a, 1992b; Colbert et al. 2004; Persic et al. 2004). This criterion might misidentify some normal star-forming galaxies with a large population of high-mass X-ray binaries (HMXBs) that produce a flat X-ray spectrum (Colbert et al. 2004; see also Fig. 2 in Alexander et al. 2005a), and might also misidentify low-luminosity AGNs whose X-ray luminosity can be lower than 10^{42} erg s^{-1}.

There are three sources with an absorption-corrected luminosity below 10^{42} erg s^{-1}, sources XMDS seq. 178, 842 (aka Arp 54), and 1248. Sources XMDS seq. 178 and 1248 are characterized by low column densities, 22×10^{20} and 2.6×10^{20} cm^{-2} (consistent

with the Galactic value), and hardness ratios, -0.43, and -0.54, respectively. However, source XMDS seq. 842 ($z_{\rm spec} = 0.043$) has a hardness ratio of 0.16, which implies a column density of 1.78×10^{22} cm^{-2}. Because of its hard X-ray spectrum, source XMDS seq. 842 is included in the AGN sample that will be investigated in the following sections. The classification of source 178 is also dubious because its optical/X-ray flux ratio $[\log(F_{0.5\text{--}10\,\rm keV}/F_R) \simeq -0.49]$ is consistent with those typical of unobscured AGNs $[-1 < \log(F_{0.5\text{--}10\,\rm keV}/F_R) < 1$; Akiyama et al. 2003]. Indeed in Paper II, where star-forming galaxies are identified based on the optical/X-ray flux ratio, XMDS seq. 178 is considered an AGN and XMDS seq. 842 is considered a star-forming galaxy. Here we prefer to adopt a criterion which is based only on intrinsic X-ray properties (luminosity and $N_{\rm H}$) rather than flux ratios that are redshift-dependent. Thus, we consider XMDS seq. 178 and 1248 to be normal star-forming galaxies and XMDS seq. 842 an AGN. Sources XMDS seq. 178 and 1248 will not be taken into account in the following analysis, which will focus only on the AGN population (132 sources in total, and 117 in sample A).

The fractions of AGNs in the three SED classes thus become $33^{+5}_{-1}\%$ AGN1s, $50^{+6}_{-11}\%$ AGN2s, and $17^{+9}_{-6}\%$ SFs.

4. AVERAGE SEDs OF THE THREE AGN SED CLASSES

After deriving the luminosity SEDs in νL_ν for each source assuming the source photometric redshift, or spectroscopic redshift if available, average normalized rest-frame SEDs, from the X-ray to the mid-IR, were obtained from all AGNs in sample A (117 sources) divided by class (SF, AGN2, and AGN1). The average SEDs are shown in Figure 5. We normalize the SEDs at 1 μm rest frame assuming the best-fit template for each source, in a similar way the median QSO template in Elvis et al. (1994) was obtained. This choice of wavelength is well suited to investigate separately the SED dispersion of the main emitting components in AGNs, the accretion disk and the stars in the optical and the dust in the infrared. The average SEDs are derived from the normalized rest-frame SEDs by taking the mean of the logarithm of the wavelength and the weighed mean of the luminosity in $\log(\nu L_\nu)$ in 0.3 wide bins. Smaller bins were chosen if more than 40 data points were available or wider bins to include at least 10 points. The weights are based on the luminosity uncertainties. Upper limits in the optical and infrared are taken into account by assuming the upper limit to the luminosity and a logarithmic uncertainty equal to twice the maximum logarithmic uncertainty of each source. Upper limits to the X-ray luminosities are taken into account by assuming as luminosity the 1 σ luminosity value and a logarithmic uncertainty equal to twice the maximum logarithmic uncertainty observed in the X-rays for that source. The average SF, AGN2, and AGN1 SEDs contain 15, 29, and 20 bins, respectively, and are obtained by averaging the rest-frame SEDs of 20 SFs, 59 AGN2s, and 38 AGN1s. The average SEDs are shown in Figure 5 as thick black curves, 1 and 2 σ dispersion are shown as gray shaded areas. Since the redshift distribution of the sample is broad, up to $z \geq 3.5$, and the majority of the sample has $z \sim 1$, the observed X-ray data sample rest-frame energies up to 45 keV for the highest z sources and up to 20 keV for the majority of the sample. Thus, the average SEDs sample rest-frame energies up to 20 keV.

The global SEDs, from X-ray to infrared, show a wide dispersion in each class. Since they are normalized at 1 μm, this dispersion is more pronounced at X-ray wavelengths. The average SEDs of the three classes show some clear differences. The average SEDs become increasingly blue in the optical–near-IR ($\lambda^{\rm rest} \leq 1$ μm), red in the IR ($\lambda^{\rm rest} \simeq 1$–10 μm), and soft in the
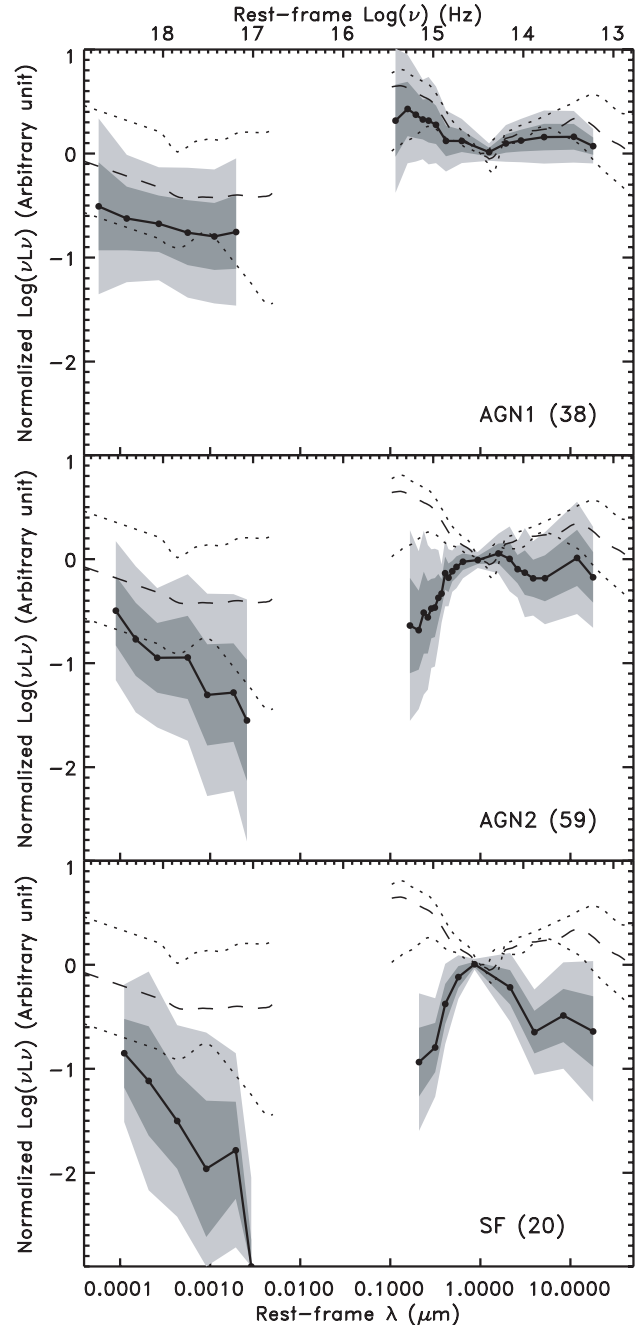

Fig. 5.—Normalized at 1 μm average rest-frame X-ray–mid-IR SEDs in $\log(\nu L_\nu)$ vs. $\log \lambda$ (*filled circles connected by straight lines*) of AGNs classified as AGN1 (38 sources, *top*), AGN2 (59 sources, *middle*), and SF (20 sources, *bottom*). The light and dark shaded areas correspond to 2 and 1 σ dispersion, respectively. Note that the X-ray luminosities are not corrected for absorption. The black thin curves represent the median (*dashed curves*) and $\pm 90\%$ dispersion (*dotted curves*) QSO template by Elvis et al. (1994).

X-rays in the sequence SF $\rightarrow$ AGN2 $\rightarrow$ AGN1 (Fig. 5, *from bottom to top*). The average SEDs are compared with the median QSO template of optically selected quasars (Elvis et al. 1994) in Figure 5. The average AGN1 SED is redder in the optical than Elvis's template, with only the bluest sources being consistent with Elvis's template. The redder optical SED of the AGN1s compared to Elvis's template suggests that these sources might include some reddened type 1 AGNs (Wilkes et al. 2002, 2005; Gregg et al. 2002; Glikman et al. 2004; Urrutia et al. 2005). Indeed, the observed range of extinction for AGN1s in the V band

is 0.0−0.55, and the median value is 0.40 (see Table 1). The SF and AGN2 optical SEDs are almost identical and significantly redder than the AGN1 optical SEDs. The observed different shape suggests that the origin of the optical emission is different in AGN1 sources from those in AGN2 and SF sources, rather than suggesting the effect of reddening on an AGN spectrum. The AGN2 and SF optical emission is likely dominated by the host-galaxy emission in most of the cases.

The near- and mid-IR ($\lambda \simeq 1$–$20\ \mu m$) average SEDs of AGN1s and AGN2s are consistent with each other at $1\ \sigma$ level, and both are redder than the SF average SED. The mid-IR SED of AGN1s and AGN2s are consistent with being dominated by AGN-heated hot dust emission, while in SFs, the host galaxy dominates. The mid-IR SED of Elvis's template is consistent with the average AGN1 mid-IR SED and redder than the average AGN2 mid-IR SED.

We show X-ray luminosities with no correction for intrinsic or Galactic absorption. AGN1s show on average softer X-ray spectra than do SFs and AGN2s, although there is a significant dispersion. The observed average spectra are consistent with increasing absorption in AGN2s compared to AGN1s, and in SFs compared to AGN2s.

Compared to Elvis's template, the normalized X-ray luminosity $[L_X/L(1\ \mu m)]$ of AGN1s is more than 2 times lower. This difference might be due to a well-known bias in Elvis's QSO sample which favors sources with strong X-ray/optical luminosity ratios and detections in the soft X-rays (Wilkes & Elvis 1987; Elvis et al. 1994).

The observed differences in the optical and IR SEDs of the three classes are mainly a consequence of the spectral classification. However, the SED classification is independent of the X-ray properties; therefore, the differences in the X-ray average spectra indicate that harder X-ray spectra are observed in more obscured AGNs.

5. LUMINOSITIES AND X-RAY ABSORPTION VERSUS AGN SED CLASS

The absorption-corrected rest-frame broadband X-ray luminosities are compared to the intrinsic column densities in Figure 6 for the entire AGN sample (132 sources). Filled symbols represent sources in sample A (117 sources), and open symbols represent sources in sample B (15 sources). Upper limits to the column density are adopted for sources with an observed column density lower or consistent with the Galactic value. The upper limit to the column density is derived from the Galactic value after applying the correction for redshift $[N_H^{Gal}(1+z)^{2.6}]$. Median luminosity values for each class, derived from sample A, are shown with dashed lines. The absorption-corrected rest-frame X-ray luminosities of AGN1s are on average more than 10 times those of SFs, while those of AGN2s show intermediate values. No correlation with the intrinsic absorption measured in the X-rays is observed. The paucity of heavily absorbed ($N_H \geq 10^{23}\ cm^{-2}$) sources at luminosities below $10^{44}\ erg\ s^{-1}$ is due to a selection effect because they would be too faint in the X-rays to be detected above our selection threshold.

Note that the area (1 deg^2) of this survey provides a large sample of highly luminous ($L_{0.5-10\ keV}^{corr} > 10^{45}\ erg\ s^{-1}$) AGNs (21 sources). As commonly found in X-ray–selected samples where unabsorbed type 1 AGNs dominate the most luminous population (Ueda et al. 2003; Akylas et al. 2006), we also find a larger fraction of AGN1s at higher X-ray luminosities. The fraction of AGN1s increases from 22% at $L_{0.5-10\ keV}^{corr} < 10^{45}\ erg\ s^{-1}$
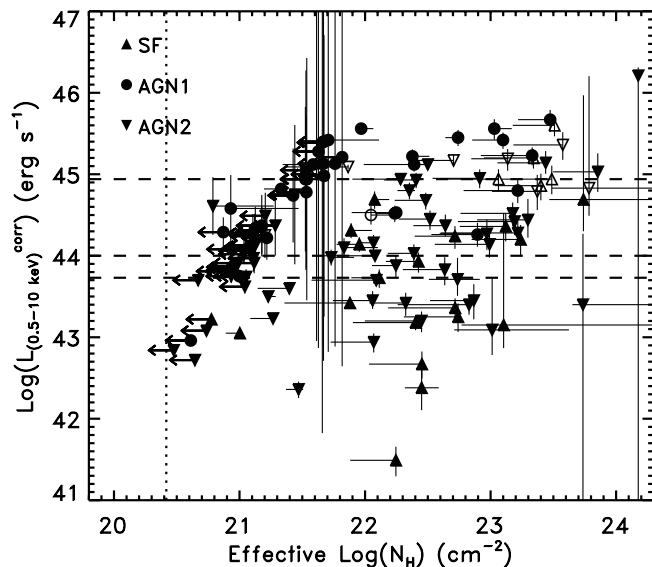

FIG. 6.—Rest-frame X-ray luminosities corrected for absorption as a function of the effective column density measured in the X-ray for the whole sample (*open and filled circles*). Filled symbols represent sources in sample A, and open symbols represent sources in sample B (see § 4). Different symbols correspond to the three SED classes: *circles*, AGN1; *inverted triangles*, AGN2; *triangles*, SFs. The dashed lines represent median values of the absorption-corrected X-ray luminosities for the three classes. The vertical dotted line indicates the Galactic value. [*See the electronic edition of the Journal for a color version of this figure.*]

to 81% at $L_{0.5-10\ keV}^{corr} \geq 10^{45}\ erg\ s^{-1}$. A detailed discussion on the fraction of unobscured (AGN1s) and obscured (AGN2s + SFs) AGNs as a function of X-ray luminosity and a comparison with previous results is reported in Paper II. Paper II also discusses the uncertainty of these estimates due to the large corrections in luminosity and column density for sources at high redshifts and the properties of absorbed QSOs ($N_H \geq 10^{22}\ cm^{-2}$ and $L_{2-10\ keV}^{corr} > 10^{44}\ erg\ s^{-1}$). It is interesting to note the lack of SF sources in sample A at high X-ray luminosities, $>10^{45}\ erg\ s^{-1}$. This indicates that powerful AGNs always dominate in the IR and are, therefore, identifiable as AGNs at those wavelengths. Thus, IR surveys can potentially be used to identify and study the most luminous AGNs. There are, however, two sources in sample B (XMDS seq. 403 and 449) classified as SFs at high luminosities ($L_{2-10\ keV}^{corr} > 10^{45}\ erg\ s^{-1}$). Since they belong to sample B, they are not included in the analysis (Fig. 6, *open triangles*). Deeper multiwavelength observations are necessary to better characterize these sources (classification and redshift) and verify their high X-ray luminosities.

The mid-IR luminosity is compared with the column density measured in the X-rays in Figure 7. The majority of AGN1s show predominantly high mid-IR luminosities ($\geq 10^{45}\ erg\ s^{-1}$), similar to the distribution of the X-ray luminosities, while SFs show mostly low mid-IR luminosities ($<10^{44.5}\ erg\ s^{-1}$), and AGN2s show intermediate values (10^{44}–$10^{45.5}\ erg\ s^{-1}$) overlapping with those of the other two classes. As for the X-ray luminosities, the mid-IR luminosities of the objects in each class do not show any obvious correlation with the intrinsic absorption measured in the X-rays.

In the next sections, we will investigate whether the observed multiwavelength properties of the three classes can be simply explained by different luminosities, dust extinction, or orientation effects. These parameters will be investigated separately for each AGN class by analyzing the mid-IR and X-ray luminosity ratio,
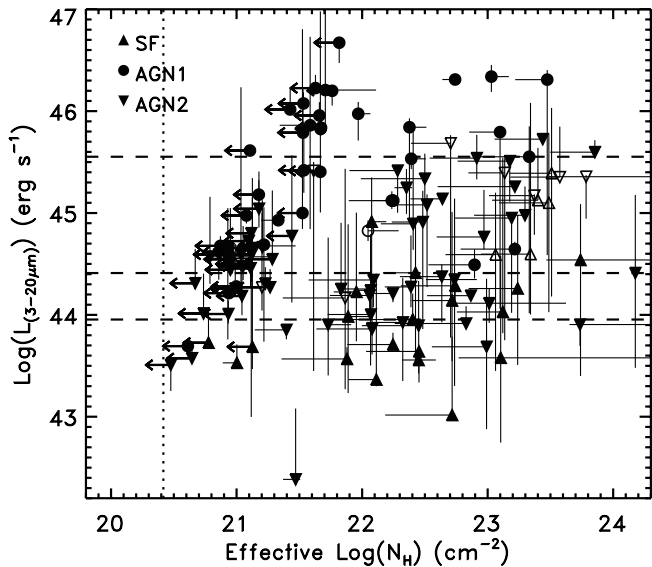
Fig. 7.—Same as Fig. 6, but comparing mid-IR luminosity with the effective column density measured in the X-rays. [*See the electronic edition of the Journal for a color version of this figure.*]
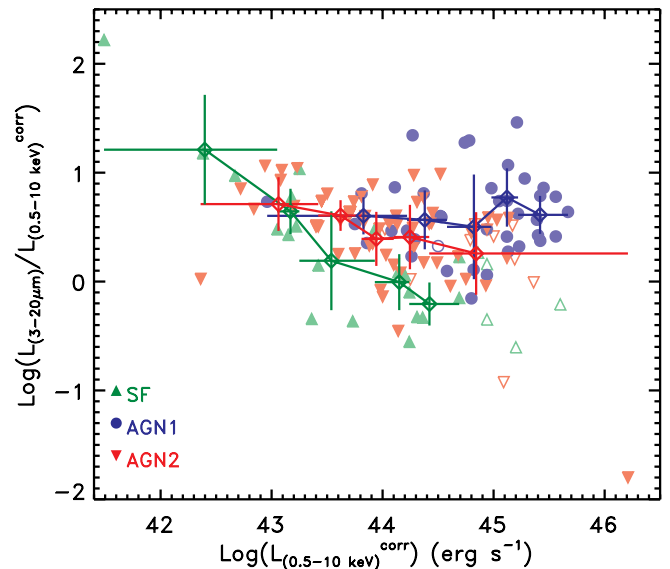

Fig. 8.—Ratio between the mid-IR and the absorption-corrected broadband (0.5–10 keV) rest-frame X-ray luminosity as a function of the absorption-corrected broadband (0.5–10 keV) rest-frame X-ray luminosity. Symbols are as in Fig. 6. The average ratios in bins of intrinsic X-ray luminosity derived for sample A (*filled symbols*) are shown as diamonds and connected by solid lines. The colors correspond to the three SED classes: *blue symbols and lines*, AGN1; *red symbols and lines*, AGN2; *green symbols and lines*, SF.

the dependence of the SEDs on the X-ray luminosity, and that of the IR colors on the luminosity and dust extinction.

6. THE RANGE OF MID-IR/X-RAY LUMINOSITY RATIOS

The nuclear mid-IR continuum in AGNs is due to reprocessing of the AGN emission by circumnuclear dust, e.g., the putative torus, and is thus function of both the AGN luminosity and the distribution of the obscuring matter. The dust covering factor in AGNs can be investigated by comparing the ratio between the mid-IR continuum (reradiation) and the intrinsic X-ray emission. A lower mid-IR/X-ray luminosity ratio is expected in highly luminous AGNs if the dust inner radius recedes (Lawrence 1991) and the torus height is constant, and in type 2 sources where the torus is seen edge-on because of mid-IR absorption (Granato et al. 1997). However, studies on Seyfert 1 and Seyfert 2 galaxies (Lutz et al. 2004; Horst et al. 2006), and type 2 QSOs (Sturm et al. 2006) where the dust covering factor is estimated from the $L_{\text{mid-IR}}/L_{2-10\,\text{keV}}^{\text{corr}}$ luminosity ratio (where $L_{\text{mid-IR}}$ is the monochromatic luminosity at 6 or 12 μm), have not found any dependence on AGN type, absorption, or X-ray luminosity.

In Figure 8, we compare the mid-IR/X-ray luminosity ratio with the absorption-corrected X-ray luminosity for the three AGN classes. In order to investigate whether there is a trend with the X-ray luminosity or the AGN class, we regrouped the data for each class in five bins with the same number of sources per bin for each class, and derived the average ratio. The average values are derived only for sample A (*filled symbols*) and are shown as diamonds connected by solid lines. For clarity, we show the data of the single sources without uncertainties. Similarly to previous studies (Lutz et al. 2004; Horst et al. 2006; Sturm et al. 2006), we find that the mid-IR/X-ray luminosity ratio is characterized by a wide dispersion and does not depend on the AGN class or the X-ray luminosity. The only exception is in a trend observed for the SF class to have a decreasing mid-IR/X-ray luminosity ratio at increasing X-ray luminosities. Some models predict smaller dust covering factors, or lower mid-IR/X-ray luminosity ratios, in more luminous sources. However, according to these models, this effect should be observed in all AGN classes and at extreme X-ray luminosities, but the mid-IR/X-ray luminosity

ratio in AGN1s and AGN2s is constant and low ratios are also observed in SFs at moderate X-ray luminosities ($\simeq 10^{43.5}$ erg s^{-1}) as shown in Figure 8.

In order to further investigate whether there is a dependence with luminosity, and whether previous studies did not cover a broad enough range of parameters (X-ray luminosities, spectral types) to observe such a trend, we produce a similar diagram using data from the literature. Instead of the integrated mid-IR luminosity we use the monochromatic 6 μm luminosity and the absorption-corrected hard (2–10 keV) X-ray luminosity because these are available for all sources in the literature. The mid-IR/X-ray ratios as a function of X-ray luminosities from various AGN samples (Borys et al. 2005; Sturm et al. 2006; Lutz et al. 2004; Weedman et al. 2006) are shown in Figure 9. In addition to the literature data, we report the average trend for the three AGN classes studied here. In this case, the average values were derived using the monochromatic 6 μm luminosity and the absorption-corrected hard (2–10 keV) X-ray luminosity as for the literature sample. The resulting trends for our sample are consistent with the results shown in Figure 8. The literature data show a large dispersion, in agreement with our results, but no dependence on AGN type or X-ray luminosity is observed. There is a group of sources from Borys et al. (2005) with typical ratios and moderate X-ray luminosities. These sources are submillimeter-detected AGNs whose optical-IR emission is mainly dominated by the host galaxy, similar to the SF class. The X-ray emission of these sources is faint, $L_{2-10\,\text{keV}}^{\text{corr}} \simeq 10^{42.5}-10^{44.2}$ erg s^{-1}, and they are characterized by low or moderate accretion rates, $dM/dt \simeq 0.01-0.80$ (Alexander et al. 2005a).

The comparison with the ratios from the literature samples confirms that the mid-IR/X-ray luminosity ratio in AGNs is characterized by a broad dispersion and that there is no dependence with the X-ray luminosity. At low and moderate X-ray luminosities some AGNs are characterized by large mid-IR/X-ray ratios because of contribution from the host galaxy to the mid-IR luminosity. In SFs, the AGN mid-IR emission is generally fainter
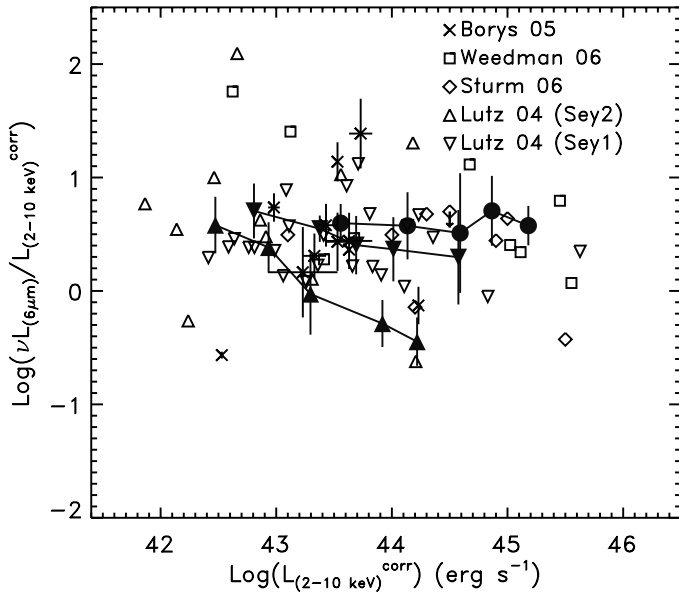
Fig. 9.—Ratio between the 6 μm and the absorption-corrected hard-band (2–10 keV) rest-frame X-ray luminosity as a function of the absorption-corrected hard-band (2–10 keV) rest-frame X-ray luminosity: *open inverted triangles and open triangles*, Seyfert 1s and Seyfert 2s from Lutz et al. (2004); *diamonds*, type 2 QSOs (Sturm et al. 2006); *open squares*, absorbed AGNs (Weedman et al. 2006); *crosses*, submillimeter-detected AGNs (Borys et al. 2005). The average ratios in bins of X-ray luminosity derived for sample A are shown connected by solid lines as filled circles, filled inverted triangles, and triangles, for the three SED classes, AGN1, AGN2, and SF, respectively. [*See the electronic edition of the Journal for a color version of this figure.*]

relative to the absorption-corrected X-ray luminosity, compared to AGN1s and AGN2s. The host-galaxy emission into the mid-IR can increase the mid-IR/X-ray ratios in SFs and make them consistent with or even larger than those observed in AGN1s and AGN2s, but in some cases, the mid-IR/X-ray ratios can be 10 times lower, as observed in the Borys et al. (2005) sample. However, it is still not clear whether the observed low ratios are due to absorption of the mid-IR AGN emission or are intrinsic. Lower intrinsic ratios might imply different dust properties (geometry, distribution, and optical depth). For example, a low mid-IR/X-ray ratio could be indicative of a lack of hot dust, as in a case in which the dust is located at a relatively large distance from the central heating source, e.g., 10 pc (Ballantyne et al. 2006). In this case, a dependence of mid-IR/X-ray ratio with the X-ray luminosity would not be expected.

7. SEDs AS A FUNCTION OF LUMINOSITY

In § 4, we compared the normalized SEDs of the three classes. Here we investigate whether the average SEDs vary with the AGN luminosity. We use the absorption-corrected broadband X-ray luminosity, $L_{0.5-10\,\mathrm{keV}}^{\mathrm{corr}}$, to separate each class (SF, AGN2, and AGN1) in three groups, sources with (1) $L_{0.5-10\,\mathrm{keV}}^{\mathrm{corr}} < 10^{44}$ erg s^{-1}, (2) $L_{0.5-10\,\mathrm{keV}}^{\mathrm{corr}} = 10^{44}$–$10^{44.64}$ erg s^{-1}, and (3) $L_{0.5-10\,\mathrm{keV}}^{\mathrm{corr}} > 10^{44.64}$ erg s^{-1}. The luminosity values that define the three groups correspond to the value that separates Seyferts and quasars, $L_{0.5-10\,\mathrm{keV}}^{\mathrm{corr}} = 10^{44}$ erg s^{-1}, and $L_{0.5-10\,\mathrm{keV}}^{\mathrm{corr}} = 10^{44.64}$ erg s^{-1} corresponds to the median luminosity of all sources with $L_{0.5-10\,\mathrm{keV}}^{\mathrm{corr}} > 10^{44}$ erg s^{-1}. Four AGN1s, 29 AGN2s, and 12 SFs are included in group 1; 10 AGN1s, 20 AGN2s, and 8 SFs in group 2, and 24 AGN1s, 10 AGN2s, and 2 SFs in group 3. The average SEDs of each class and group are shown in Figure 10. On the left side we show the SEDs regrouped by X-ray luminosity and on the right side by class. Note that the average absorption-

corrected X-ray luminosities of each class within a group can differ by up to a factor of 2. Elvis's median QSO template is shown for comparison. The average absorption-corrected X-ray luminosities are shown as dashed lines at 0.5–10 keV in the rest frame.

The optical–near-IR (0.4–2 μm) luminosities of the three classes in the lowest X-ray luminosity group (group 1) are all consistent within the 1 σ dispersion (Fig. 10a). However, the SEDs are characterized by different shapes: flat for the AGN1s, consistent with AGN emission at all wavelengths; optically red and flat in the IR for the AGN2s, consistent with being dominated by emission from the host galaxy or by a reddened AGN in the optical and from the AGN in the IR; and optically red and blue in the IR for the SFs, consistent with being dominated by emission from the host galaxy at all wavelengths. In the X-rays, AGN1s and AGN2s show soft spectra, consistent with no absorption, while SFs show a hard spectrum. The sources in this class are more than 10 times less luminous than Elvis's QSO median template at all wavelengths.

In group 2 (Fig. 10c), the optical-IR luminosities of the three classes show properties similar to those in group 1. However, the difference in luminosity at short ($\lambda < 0.4\ \mu$m) and long ($\lambda > 2\ \mu$m) wavelengths in the three classes increases. The X-ray spectra are all similar and consistent with the canonical slope ($\alpha_{\mathrm{X}} = 0.7$). The difference in luminosity with Elvis's QSO median template is lower than in group 1, but they are still from 3 to 10 times less luminous.

In group 3 (Fig. 10e), the trend observed in the two previous groups is confirmed: the optical-IR luminosities of the three classes separate further, with the AGN1s being from 10 to 100 times more luminous than the SFs. In the X-rays, a large difference is observed between the absorption-corrected luminosities and the observed values in AGN2s and SFs, indicating large absorption, while no indication of X-ray absorption is seen in AGN1s. The AGN1 luminosities are now consistent with Elvis's QSO median template in the optical and X-ray, and higher in the IR.

The average SEDs in each class also show a change in the overall shape as a function of X-ray luminosity (see Fig. 10, *right*).

AGN1s (Fig. 10b) have overall similar IR, optical, and X-ray SEDs at all luminosities, with only a slightly redder SED at $\lambda > 1\ \mu$m and less soft X-ray spectra at higher X-ray luminosities. The optical-IR luminosities scale with the X-ray luminosities, both uncorrected and corrected for absorption.

The AGN2s (Fig. 10d) show a clear change in the optical-IR SED as the X-ray luminosity increases, with the overall SED becoming redder. The most plausible explanation for this change is increasing contribution from hot dust continuum emission associated with the AGN, e.g., the putative torus, or less contribution from the host galaxy. In the lowest luminosity group, the host galaxy still dominates, but at large luminosities its emission is significantly lower than that of the AGN. It is difficult to characterize the host-galaxy emission in the mid-IR because it can change dramatically for an elliptical, late spiral, or starburst galaxy. In all cases the host-galaxy light peaks in the near-IR, $\sim$1–2 μm, where the AGN light has a minimum (Sanders et al. 1989). At longer wavelengths the host-galaxy emission can decrease or increase, according to the galaxy type, and the AGN contribution increases. Thus, the total spectrum goes from blue if the host dominates to flat if the two contributions are similar to red when the AGN dominates. We can expect to see this trend for AGNs of increasing luminosity if the host-galaxy luminosity is fixed or does not scale with the AGN luminosity. The X-ray spectra of the AGN2s change from soft to hard as the luminosity increases. It is interesting to note that the AGN mid-IR luminosity does not scale with the absorption-corrected luminosity. Indeed,
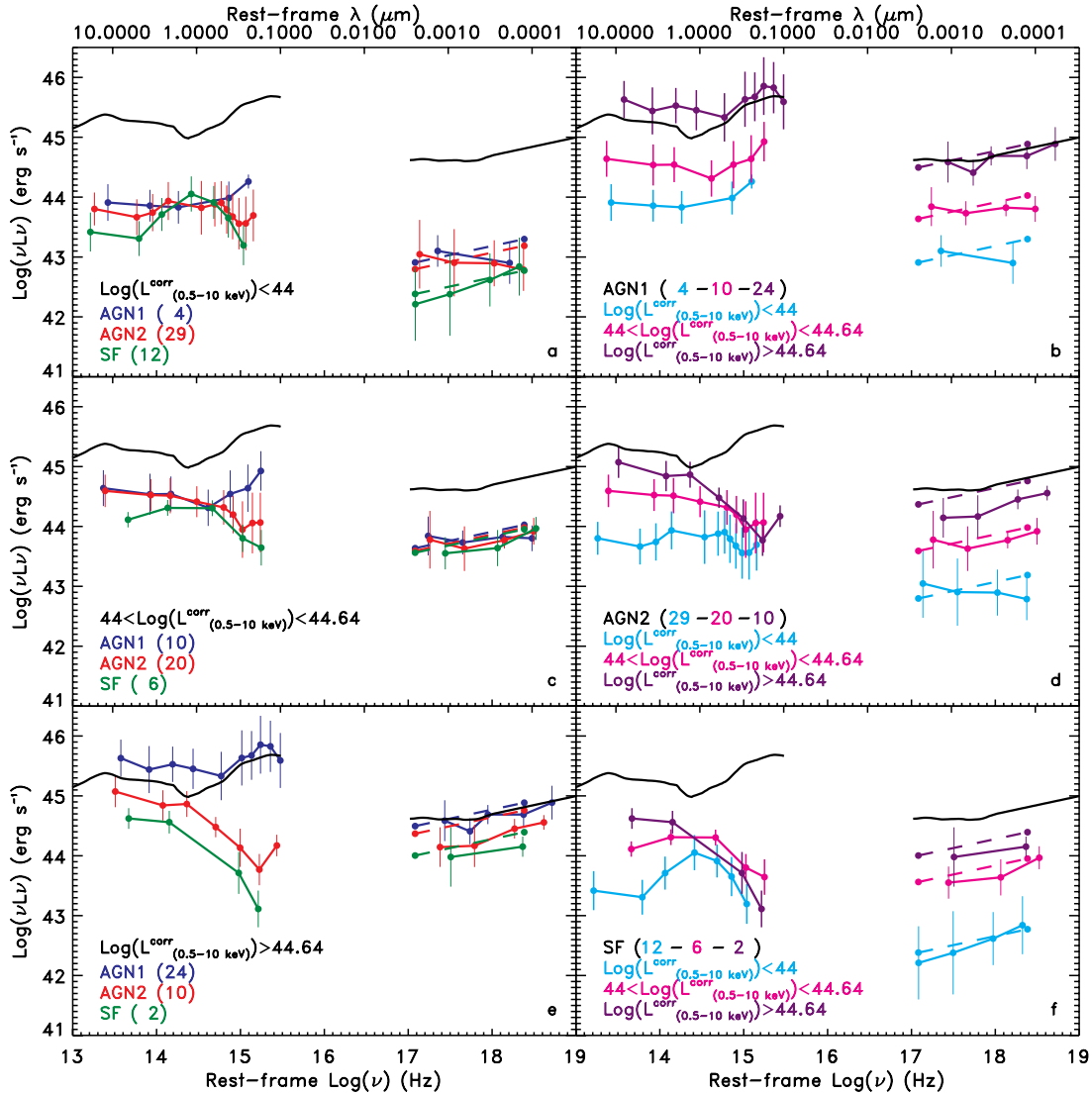
Fig. 10.—*Left:* Average rest-frame mid-IR–X-ray SEDs in log (νL_ν) vs. log ν of all AGNs with absorption-corrected broadband X-ray luminosity lower than (*a*) 10^{44} erg s^{-1}, (*c*) 10^{44}–$10^{44.64}$ erg s^{-1}, and (*e*) >$10^{44.64}$ erg s^{-1} shown as filled circles connected by solid lines. Uncertainties correspond to the mean absolute deviation. Note that the X-ray SEDs are not corrected for absorption. The average SEDs for AGNs classified as SFs are shown in green, for AGN2s in red, and for AGN1s in blue. The dashed lines represent the average absorption-corrected 0.5–10 keV rest-frame X-ray luminosities for each AGN class and luminosity group. *Right:* Average rest-frame mid-IR–X-ray SEDs in log (νL_ν) vs. log ν of (*b*) all AGN1s, (*d*) AGN2s, and (*f*) SFs with absorption-corrected broadband X-ray luminosity below 10^{44} erg s^{-1} (*cyan circles and lines*), 10^{44}–$10^{44.64}$ erg s^{-1} (*magenta circles and lines*), and >$10^{44.64}$ erg s^{-1} (*purple circles and lines*). The number of sources used to derive the average SEDs is annotated. The black solid curve represents the median template for optically selected QSOs (Elvis et al. 1994).

the mid-IR luminosity of the most X-ray luminous AGN2s is less than twice that of those with intermediate X-ray luminosity, while the X-ray luminosity is almost 10 times higher. This suggests mid-IR absorption in more luminous sources or a lower dust covering factor.

The SFs (Fig. 10*f*) show a change in SED shape similar to that of the AGN2s. In this class, the near-IR ($\sim 1\ \mu$m) luminosity remains approximately the same in the three groups; however, the absorption-corrected X-ray luminosity is about 40 times larger in the most X-ray luminous SFs than in the less X-ray luminous ones. The decrease in mid-IR luminosity relative to the absorption-corrected X-ray luminosity with increasing X-ray luminosities discussed in § 6 is also visible here. This result is even more remarkable considering that the host galaxy contributes to the mid-IR luminosity.

The decreasing mid-IR luminosity compared to the absorption-corrected X-ray luminosity observed in the most luminous AGN2s and in the SFs is equivalent to the low mid-IR/X-ray ratios found

at high X-ray energies in SFs discussed in § 6 and shown in Figures 8 and 9. From the analysis in § 6, we concluded that the deficiency of mid-IR light is not dependent on the AGN X-ray luminosity. However, when the AGN X-ray luminosity is low the host galaxy might be luminous enough to compensate for the mid-IR deficiency, preventing low mid-IR/X-ray ratios from being observable in less luminous AGNs. Assuming that a molecular torus surrounds the nuclear source, the deficiency of mid-IR light relative to the X-ray luminosity observed in SFs and some AGN2s can be explained by lack of hot dust, larger optical depths, or large angles of the line of sight from the torus axis (Granato & Danese 1994; Granato et al. 1997).

8. THE ORIGIN OF AGN IR COLORS

Lacy et al. (2004) identified a region in IRAC color space (3.6–8.0 μm) where most of the AGNs detected in all four IRAC bands are distributed (see also Barmby et al. 2006; Stern et al. 2004; Hatziminaoglou et al. 2005). AGNs preferentially occupy
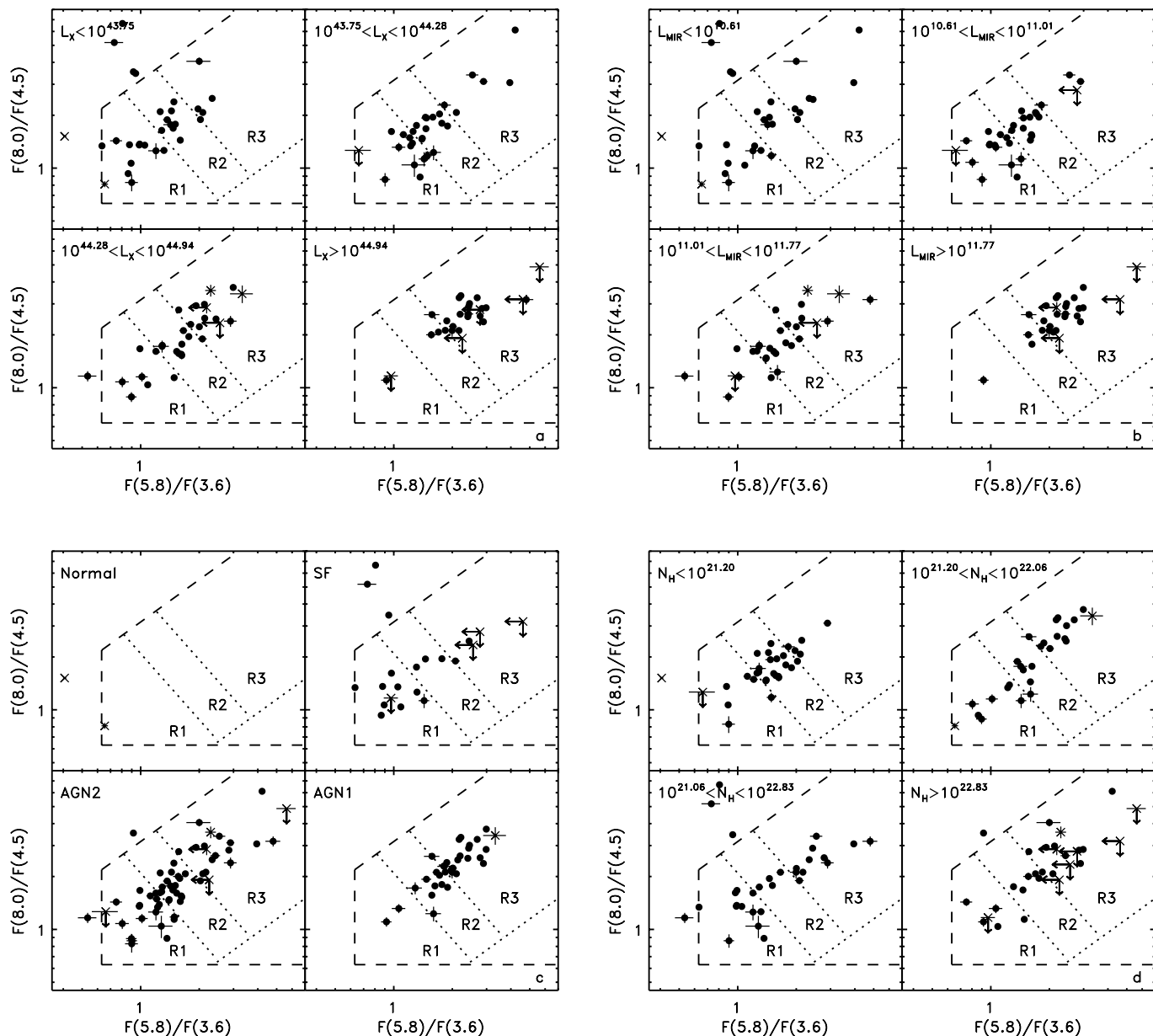
Fig. 11.—IRAC colors, $F(8.0\ \mu m)/F(4.5\ \mu m)$ vs. $F(5.8\ \mu m)/F(3.6\ \mu m)$, as in Lacy et al. (2004) for our sample. Filled symbols represent sources in sample A, and crosses represent sources in sample B. Each figure shows (a) sources with different absorption-corrected X-ray luminosity, (b) mid-IR (3–20 μm) luminosity, (c) SED class, and (d) column density as estimated in the X-rays. Each figure is divided in four panels with sources in four different subgroups as annotated. Left-pointing arrows represent 5 σ upper limits at 5.8 μm, downward-pointing arrows represent 5 σ upper limits at 8.0 μm. The region enclosed by the dashed line corresponds to the region identified by Lacy et al. (2004) where the majority of IRAC-detected AGNs lie. The dotted lines define three subregions within Lacy's region, labeled R1, R2, and R3, where the same number of sources in our sample lies. The number of sources in each group and the fraction in each region are listed in Table 2.

this region because of their red and almost featureless IR SED. Only 5 of 87 sources in sample A with detections in all four IRAC bands are not within the "AGN wedge" as defined by Lacy et al. (2004). For 15 additional objects, only an upper limit in one or more IRAC bands is available. We can therefore conclude that Lacy's criterion is satisfied by 80% of our X-ray sources in sample A observed with IRAC (this fraction is obtained with the pessimistic assumption that all the sources with IRAC limits would fall outside Lacy's wedge) or by a fraction close to 95% (97/102, if we assume that all the sources with upper limits lie within the wedge). Thus, this criterion appears to be fairly complete for a relatively bright X-ray sample such as the XMDS sample. Using the properties (SED class, luminosity, and absorption) derived for the AGNs in the

XMDS, we investigate how these affect the IRAC colors and make them so distinctive for AGNs.

In the hypothesis that different AGN types and column densities correspond to tori seen at different angles with respect to the line of sight and that the mid-IR radiation is dominated by the torus emission, a dependence of the IR colors on the AGN class (type 1 vs. type 2) and on the absorption in the X-rays is expected. In Figure 11, we reproduce Lacy's color diagram, plotting separately sources in different intervals of absorption-corrected X-ray luminosity (Fig. 11a), mid-IR (3–20 μm) luminosity (Fig. 11b), SED classification (Fig. 11c), and column density (Fig. 11d). IRAC colors are constrained for 107 of the 117 sources in sample A, and 102 satisfy Lacy's color criteria: all AGN1s and most

TABLE 2
FRACTION OF AGNs VERSUS MID-IR COLOR REDNESS

Group	N	% in R1	% in R2	% in R3
All	107 (87)	28 (25)	32 (33)	36 (36)
$L_X < 10^{43.8}$	25 (24)	37 (45)	29 (34)	11 (13)
$10^{43.8} < L_X < 10^{44.3}$	29 (21)	37 (32)	35 (34)	16 (13)
$10^{44.3} < L_X < 10^{44.9}$	26 (20)	23 (18)	26 (28)	26 (26)
$L_X > 10^{44.9}$	22 (17)	3 (5)	9 (3)	47 (48)
$L_{\text{mid-IR}} < 10^{10.6}$	24 (17)	33 (32)	21 (21)	18 (13)
$10^{10.6} < L_{\text{mid-IR}} < 10^{11.0}$	29 (23)	47 (50)	35 (31)	8 (10)
$10^{11.0} < L_{\text{mid-IR}} < 10^{11.2}$	25 (23)	17 (14)	35 (41)	21 (26)
$L_{\text{mid-IR}} > 10^{11.2}$	24 (19)	3 (5)	9 (7)	53 (52)
Normal	0 (0)	0 (0)	0 (0)	0 (0)
SF	14 (7)	30 (27)	9 (0)	5 (3)
AGN2	55 (45)	63 (64)	62 (69)	39 (35)
AGN1	33 (30)	7 (9)	29 (31)	55 (61)
$N_H < 10^{21.20}$	25 (24)	33 (41)	32 (38)	11 (13)
$10^{21.20} < N_H < 10^{22.06}$	29 (25)	33 (32)	32 (38)	21 (23)
$10^{22.06} < N_H < 10^{22.83}$	27 (16)	30 (23)	29 (21)	21 (16)
$N_H > 10^{22.93}$	21 (17)	3 (5)	6 (3)	47 (48)

NOTES.—The reported statistics refers to 107 sources for which IRAC observations are available. Of these, 87 sources are detected in all four IRAC bands, for the remaining 20 sources upper limits were adopted, 4.3, 8.3, 58.5, and 65.7 μJy at 3.6, 4.5, 5.8, and 8.0 μm, respectively. The values in parentheses refer to the subsample of 87 sources with detections in all four IRAC bands. L_X is the absorption-corrected luminosity in the 0.5–10 keV rest-frame interval in erg s^{-1}. $L_{\text{mid-IR}}$ is the mid-IR luminosity integrated between 3 and 20 μm rest frame in $L_\odot$. N_H is the intrinsic column density measured in the X-rays in cm^{-2}. R1, R2, and R3 represent three regions defined in color space by the flux ratios, $F(5.8\ \mu\text{m})/F(3.6\ \mu\text{m})$ and $F(8.0\ \mu\text{m})/F(4.0\ \mu\text{m})$. They are shown in Fig. 11. Only sources in sample A are taken into account.

AGN2s (96%) and SFs (82%). We divided the area defined by Lacy et al. (2004) into three subregions, R1, R2, and R3, that contain sources with increasing flux ratios or redness and approximately the same number of sources ($\sim$34). The equation of the line that divides regions R1 and R2 is $\log[F(8.0\ \mu\text{m})/F(4.5\ \mu\text{m})] = 0.32 - 1.25 \log[F(5.8\ \mu\text{m})/F(3.6\ \mu\text{m})]$, and the equation of the line that divides regions R2 and R3 is $\log[F(8.0\ \mu\text{m})/F(4.5\ \mu\text{m})] = 0.661 - 1.25 \log[F(5.8\ \mu\text{m})/F(3.6\ \mu\text{m})]$. In order to investigate whether any AGN property (class, X-ray luminosity, mid-IR luminosity, and X-ray absorption) is correlated with the mid-IR redness, we derived the fraction of sources with a specific property in each region. Table 2 reports the number of sources per region, including upper limits or detections only.

The position of the sources in the diagram is strongly correlated with the SED class. The fraction of AGN1s increases from R1 to R3, while most of the SFs are in R1 and most of the AGN2s in R2. The observed dependence is the opposite of what expected from AGN tori models, where redder SEDs are predicted in more obscured sources. A likely explanation for this correlation is the increasing host-galaxy contribution from AGN1s to SFs. A correlation with the IRAC colors is also observed as a function of X-ray and mid-IR luminosities, with the fraction of the most luminous sources increasing and that of the less luminous decreasing going from R1 to R3. This correlation is consistent with less host contribution in the IR in more luminous AGNs. The parameter least correlated with the IRAC colors is the column density measured in the X-rays. However, all sources in sample A outside the Lacy et al. (2004) region are X-ray absorbed.

9. RADIO LUMINOSITY VERSUS X-RAY AND MID-IR LUMINOSITIES

In star-forming galaxies, the radio and far-infrared (FIR, 42.5–122.5 μm) emission are strongly correlated (Dickey & Salpeter

1984; de Jong et al. 1985). The majority of AGNs (radio-quiet AGNs), about 90%, depending on the sample selection, follow the same correlation as star-forming galaxies, and a minority, i.e., radio galaxies and radio-loud quasars, show an excess of radio emission compared to radio-quiet objects with similar FIR emission (Sopp & Alexander 1991; Roy et al. 1998). The FIR/radio flux ratio is thus a good diagnostic tool to identify AGN activity. In recent studies, this correlation has been used by replacing the FIR emission with the 24 μm emission because the latter is more easily available for faint high-z sources thanks to *Spitzer* (Appleton et al. 2004; Higdon et al. 2005; Donley et al. 2006), although the correlation between the 24 μm and the FIR emission is characterized by a large dispersion (Brandl et al. 2006; Barger et al. 2007). The radio continuum is also correlated with the X-ray emission in AGNs (e.g., Brinkmann et al. 2000; Simpson et al. 2006). A correlation between the radio and the X-ray emission is also observed in star-forming galaxies; however, the X-ray luminosity is on average 400 times lower than in AGNs of similar radio luminosity (Ranalli et al. 2003). Here we investigate whether our data are consistent with the well-known FIR-radio and X-ray–radio correlations and whether radio data can help identify heavily obscured AGNs.

There are 32 sources in our sample detected at 1.4 GHz; six belong to sample B (three with dubious optical counterparts and three with poorly sampled SEDs). Upper limits to the radio flux are available for 68 sources (two are in sample B). Thus, there are 26 radio-detected and 66 nondetected sources in sample A. Radio data can be used to identify the presence of an AGN by looking for an excess of radio emission compared to the optical and/or the IR flux. According to Stocke et al. (1992) radio-loud AGNs are characterized by a radio/optical ratio, $R = F_{5\ \text{GHz}}/F_{2500\ \text{Å}}$, greater than 100.[13] We derive the radio flux at 5 GHz assuming a spectral index $\alpha_R = 0.8$ ($F_\nu \propto \nu^{-\alpha_R}$) and the optical flux by interpolating the observed data at the wavelength corresponding to 2500 Å rest frame. Seven sources have $R \geq 100$ (XMDS seq. 18, 58, 111, 120, 403, 747, and 1219) of which two (XMDS seq. 403 and 1219) are optically blank and five are in sample B (XMDS seq. 111, 120, 403, 747, and 1219). We also calculated the parameter q, defined as $\log(F_{24\ \mu\text{m}}/F_{20\ \text{cm}})$, and identified a radio excess in all sources with $q < 0.0$ (Donley et al. 2005). Five sources satisfy this criterion, XMDS seq. 403, 738, 747, 1219, and 1246. Three sources are selected by both criteria (XMDS seq. 403, 747, and 1219); for two (XMDS seq. 111 and 120) the q-parameter cannot be derived because there is no IR coverage. In summary, the presence of an excess of radio emission remains uncertain in six sources for which only one of the two criteria is satisfied or can be applied, XMDS seq. 18, 58, 111, 120, 738, and 1246, and it is confirmed by both criteria in three sources, XMDS seq. 403, 747, and 1219.

In Figures 12 and 13, we investigate the correlation between the radio luminosity and the mid-IR and X-ray luminosity by comparing the ratio between the rest-frame integrated mid-IR (3–20 μm) and absorption-corrected rest-frame broadband (0.5–10 keV) X-ray luminosities and the rest-frame radio luminosity at 1.4 GHz with the rest-frame radio luminosity at 1.4 GHz for the 32 X-ray sources that are detected at radio wavelengths. We show the luminosity ratio to remove the redshift effect. The nine radio-loud objects are shown as plus signs, and crosses are overplotted on the three more secure radio-loud AGNs. The six

---

[13] The definition of radio-loud based on the parameter $R = F_{5\ \text{GHz}}/F_{2500\ \text{Å}}$ depends on whether the parameter R is k-corrected and on what spectral indices are assumed in the optical and in the radio. Typical values are $\log R < 0.5$ for radio-quiet and $\log R > 2$ for radio-loud objects (Stocke et al. 1992).
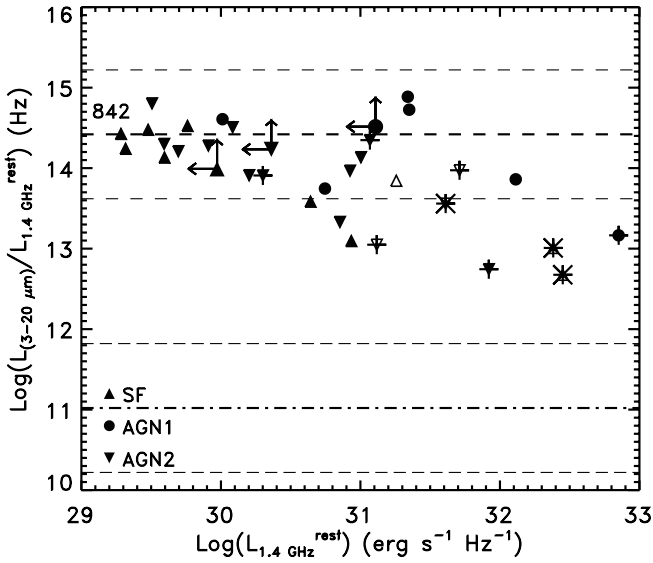
Fig. 12.—Ratio between the rest-frame mid-IR (3–20 μm) luminosity and the rest-frame 1.4 GHz radio luminosity vs. the rest-frame 1.4 GHz radio luminosity. Symbols are as in Fig. 6. The thick dashed line represents the L(mid-IR)-L(radio) correlation derived from the L(FIR)-L(radio) correlation observed for radio-quiet AGNs and star-forming galaxies (Sopp & Alexander 1991; Ranalli et al. 2003). The thin dashed lines represent the dispersion associated with the conversion from the FIR luminosity to the mid-IR luminosity. The thick dot-dashed line represents the L(mid-IR)-L(radio) correlation derived from the L(FIR)-L(radio) correlation observed for radio-loud AGNs (Sopp & Alexander 1991). Plus signs represent nine sources classified as radio-loud based on the radio/optical or radio/IR flux ratio; crosses are overplotted on the three sources that satisfy both criteria (see text). The upward- and left-pointing arrows represent the median radio luminosity and luminosity ratio obtained from the nondetected sources in each group. [*See the electronic edition of the Journal for a color version of this figure.*]
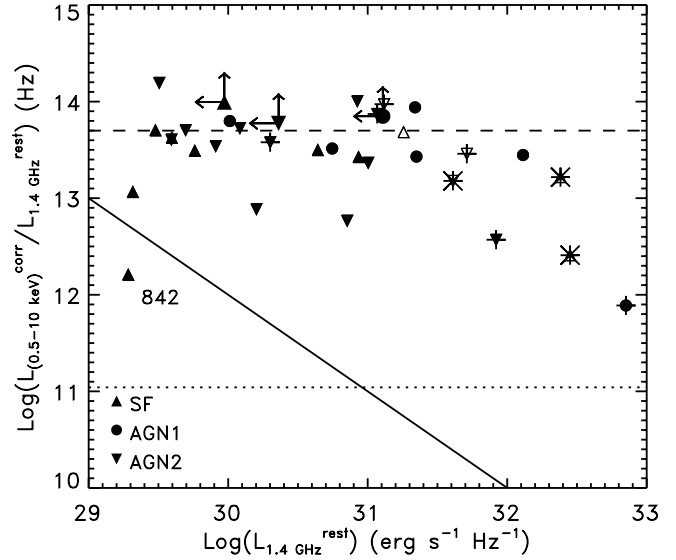
Fig. 13.—Ratio between the absorption-corrected rest-frame broad (0.5–10 keV) X-ray luminosity and the rest-frame 1.4 GHz radio luminosity vs. the rest-frame 1.4 GHz radio luminosity. Symbols are as in Figs. 6 and 12. The dashed line represents the L(X-ray)-L(radio) correlation derived for radio-quiet AGNs in the *ROSAT*-FIRST survey (Brinkmann et al. 2000). The dotted line represents the L(X-ray)-L(radio) correlation derived for star-forming galaxies (Ranalli et al. 2003). The solid diagonal line corresponds to a fixed X-ray luminosity of 10^{42} erg s^{-1}. [*See the electronic edition of the Journal for a color version of this figure.*]

sources in sample B are shown as open symbols. Although these sources are classified as radio-loud by the criteria described above, based on their radio–to–mid-IR and radio/X-ray luminosity ratios, it would be more appropriate to consider them as radio-intermediate AGNs. For clarity we do not report sources that are not radio-detected, but for each class we show the median upper limit to the radio luminosity and to the luminosity ratio obtained from the nondetected sources.

In Figure 12, we test whether our sample shows the same correlation between the FIR (60 μm) luminosity and the radio luminosity at 5 GHz as observed in local radio-quiet and radio-loud AGNs (Sopp & Alexander 1991). We converted the monochromatic luminosity at 5 GHz to that at 1.4 GHz assuming a radio spectral index $\nu_R = 0.5$ ($I \propto \nu^{-\alpha_R}$) as in Sopp & Alexander (1991) and the monochromatic luminosity at 60 μm to the mid-IR luminosity using the equation, $L_{3-20\,\mu m} = (0.4 \pm 0.8)\nu L_{60\,\mu m}$, derived from the templates that fit the SEDs of our sample. The expected relationships are $\log L_{1.4\,GHz} = \log L_{3-20\,\mu m} - 11.02 \pm 0.8$ for the radio-loud sources and $\log L_{1.4\,GHz} = \log L_{3-20\,\mu m} - 14.42 \pm 0.8$ for the radio-quiet ones, where $L_{1.4\,GHz}$ is in ergs per second per hertz and $L_{3-20\,\mu m}$ in ergs per second. The two relationships are shown in Figure 12 as thick dashed (radio-quiet) and dot-dashed (radio-loud) lines. The thin lines represent the dispersion associated with the conversion from $\nu L_{60\,\mu m}$ to $L_{3-20\,\mu m}$. Most of the radio-quiet sources in our sample follow the expected correlation. The Spearman rank correlation coefficient between the radio and the mid-IR luminosities is $\rho_S = 0.84$ and the probability is 1×10^{-07}. The lowest luminosity ratios are observed for the sources considered radio-loud based on the optical/radio or the IR/radio flux ratios; however, they all show higher ratios than expected for radio-loud sources (Fig. 12, *dot-dashed line*).

We find a similarly strong correlation between the rest-frame radio luminosity at 1.4 GHz and the absorption-corrected rest-frame broadband (0.5–10 keV) X-ray luminosity (Spearman rank correlation coefficient $\rho_S = 0.91$ and probability of its deviation from zero $= 1.9 \times 10^{-10}$). We compared the measured relationship with that found for radio-quiet AGNs (Simpson et al. 2006; Brinkmann et al. 2000; Fig. 13, *dashed line*). The expected relationship has been derived from the correlation observed between the monochromatic luminosities at 5 GHz and at 2 keV of a sample of radio-quiet ($\log R \leq 1$) sources from the *ROSAT*-FIRST sample (Brinkmann et al. 2000). The radio luminosity has been converted to $L_{1.4\,GHz}$ assuming a radio spectral index of 0.7, and the X-ray luminosity at 2 keV has been converted to $L_{0.5-10\,keV}$ assuming a spectral index $\alpha_X = 0.8$ as assumed in Brinkmann et al. (2000). The final relationship is $\log L_{1.4\,GHz} = \log L_{0.5-10\,keV} - 13.91$ (see also Simpson et al. 2006) and is shown as a dashed line in Figure 13. The sources in our sample show luminosity ratios consistent with those expected based on this relationship.

The agreement with correlations derived from samples selected in different energy bands, and at different flux limits, reinforces the validity of these correlations. Since the radio luminosity can be considered an isotropic indicator of the nuclear unabsorbed X-ray luminosity for radio-quiet AGNs, these correlations can be used to probe the unabsorbed X-ray luminosity of radio-quiet AGNs and to identify absorption effects in X-ray observed AGNs, similar to the analysis based on the [O III] λ5007 luminosity (see, e.g., Mulchaey et al. 1994; Alonso-Herrero et al. 1997; Turner et al. 1997; Maiolino et al. 1998; Risaliti et al. 1999; Bassani et al. 1999).

The XMDS sample offers an opportunity for such an application. Source XMDS seq. 842 does not follow any of the correlations between the X-ray and the radio luminosities expected for AGNs or star-forming galaxies. Because of its low X-ray luminosity, lower than 10^{42} erg s^{-1}, the evidence for AGN activity from the X-rays in this source is only based on

the hardness of its X-ray spectrum. However, its radio/X-ray luminosity ratio is ∼10 times larger than what is expected for normal star-forming galaxies (Ranalli et al. 2003), supporting the assumption that this source is an AGN. This behavior suggests that the X-ray luminosity might be underestimated by a factor of 40, a hypothesis that would indicate that the source is Compton thick and the observed X-ray emission is only scattered light. This source will be observed with the γ-ray observatory, *INTEGRAL*, as part of a 2 Ms survey of the XMM-LSS field (Virani et al. 2005). We estimate the luminosity and expected flux in the energy range 20–100 keV, where *INTEGRAL* is sensitive, to determine whether *INTEGRAL* will be able to detect it. Assuming that the absorption-corrected rest-frame 0.5–10 keV luminosity is 40 times higher, the derived luminosity is $L_{20-100\,\mathrm{keV}} = 2.9 \times 10^{43}$ erg s^{-1}, which corresponds to an absorption-corrected flux $F_{20-100\,\mathrm{keV}}^{\mathrm{corr}} \simeq 7 \times 10^{-12}$ erg cm^{-2} s^{-1} and an observed flux $F_{20-100\,\mathrm{keV}} \simeq 6.8 \times 10^{-12}$ erg cm^{-2} s^{-1} assuming a column density of 10^{24} cm^{-2}. So far, *INTEGRAL* has not detected AGNs at these flux levels (Beckmann et al. 2006; Bassani et al. 2006); however, the long XMM-LSS exposure might be able to reveal the heavily obscured AGNs in source XMDS seq. 842 (aka Arp 54).

10. DISCUSSION

10.1. *AGN Identification through SED Fitting*

In this work, we have characterized the SEDs of a hard X-ray selected sample of AGNs. As previously found (see, e.g., Alexander et al. 2001a, 2001b, 2002; Fadda et al. 2002; Perola et al. 2004; Szokoly et al. 2004; Franceschini et al. 2005; Polletta et al. 2006), the multiwavelength SEDs of X-ray–selected AGNs show a wide variety of properties. We divide the SEDs in three broad classes, AGN1, AGN2, and SF. The fraction of AGNs that fall into the various SED classes likely depends on the sample selection, i.e., spectral window and flux limit. For example, an optically selected sample will have a larger fraction of AGN1s, and an IR-selected sample will be biased against AGNs in the SF class. A different X-ray flux limit or a selection in a different X-ray band can also alter the fraction of sources in the various classes. For example, Franceschini et al. (2005) find 39% AGN1s, 23% AGN2s, and 38% SFs in a sample of AGNs with broad X-ray fluxes $F_{0.5-8\,\mathrm{keV}} > 10^{-15}$ erg cm^{-2} s^{-1}. If the classification of the sources fitted with a Mrk 231 template in Franceschini et al. (2005) is modified from AGN1 to AGN2 as assumed here, the fractions become 15% of AGN1s, 42% of AGN2s, and 36% of SFs. The AGN1 fraction is lower than ours (15% vs. 33%), the fraction of AGN2s is slightly lower than ours (42% vs. 50%), and the fraction of SFs is twice ours (36% vs. 17%). These differences are likely due to our higher X-ray flux limit and requirement of detection in the hard X-ray band (2–10 keV). There is indeed an indication for the fraction of AGN1s to decrease and the fraction of SFs to increase at fainter X-ray fluxes (see Paper II for a more detailed analysis). The trend of having fewer AGN1s and more SFs at lower X-ray flux levels has to be confirmed and better quantified using similarly selected samples with analogous classification covering a broad range of fluxes.

Although hard X-ray samples, as that used here, provide the least biased AGN samples, some AGNs, e.g., Compton thick AGNs, are still missed. However, we do not expect the SEDs of Compton thick AGNs to fall in a separate class. Known Compton thick AGNs, both in the local universe and at high redshifts, show SEDs that are consistent with the AGN2 (e.g., Mrk 231 and NGC 1068) and SF classes (e.g., NGC 4945 and NGC 6240). From the SED analysis of a sample of X-ray–selected Compton thick

AGNs, Polletta et al. (2006) estimate that 60% of Compton thick AGNs fall in the SF class and 40% in the AGN2 class. Thus, through SED fitting we can identify a large fraction of AGNs, even Compton thick AGNs. The SED fitting technique provides an efficient AGN identification tool. The main advantage is that it is based on data that can be more easily obtained than X-ray data and spectroscopic data. Moreover, this technique identifies the same or an even higher fraction of AGNs than the spectroscopic classification. Based on the sample of 49 spectroscopically identified XMDS sources, we estimate that the SED fitting technique is able to identify AGN activity in 8 of 11 (73%) AGNs that are spectroscopically classified as star-forming galaxies, in 7 of 12 (58%) AGNs that are spectroscopically classified as type 2 AGNs, and in 25 of 26 (96%) AGNs that are spectroscopically classified as type 1 AGNs. Overall, we identify AGN activity in 40 of 49 (82%) hard X-ray selected AGNs with available spectroscopic data and in 83% (50% of AGN2s and 33% of AGN1s) in the entire X-ray sample, while optical spectroscopy identifies AGN activity in 38 sources (78%). The SED fitting technique can be applied to sources that are too faint at optical wavelengths for optical spectroscopic observations, or with emission lines that are diluted by the host-galaxy light or affected by obscuration (Moran et al. 2002; Barger et al. 2001; Rigby et al. 2006), and to sources in the redshift desert. There is evidence that these sources might represent a significant fraction of AGN samples. Thus, SED fitting represents a powerful and efficient tool to identify AGN activity in samples for which optical spectroscopic observations are unavailable or impossible to perform.

However, this technique also has some limitations. Almost half of type 2 AGNs and a third of star-forming-galaxy–like AGNs might still be missed and not identified as AGNs. Moreover, the SED classification can be misled by the more dominant host-galaxy light at optical–near-IR wavelengths as in many Seyfert 1 galaxies and thus misclassify a type 1 AGN as AGN2 or SF. These limitations might be overcome if well-sampled multiwavelength SEDs of large AGN samples in various classes with spectroscopic data become available. With such data the AGN templates can be improved and expanded and the SED fitting technique can be refined.

In the next section we discuss the nature of the AGNs that are not identified by the SED technique and by optical spectroscopy.

10.2. *The Nature of Elusive AGNs*

There are several examples of AGNs in the literature whose optical spectra or broadband SEDs resemble those of normal galaxies and are, therefore, not identified as AGNs unless probed by X-ray or radio data. We refer to these sources as elusive AGNs (Maiolino et al. 2003). These sources belong to the SF class and might have many properties in common with known categories of elusive AGNs found in the literature, such as the optically dull AGNs discovered in optical samples (Maiolino et al. 2003; Elvis et al. 1981; Rigby et al. 2005), the X-ray bright optically normal galaxies (XBONGs) discovered in X-ray samples (Comastri et al. 2002), and the type 3 QSOs found in IR-selected samples (Martínez-Sansigre et al. 2006; Leipski et al. 2007). The rich taxonomy of these categories reflects mostly the wavelengths at which they were discovered, while the scenarios proposed to explain their nature are similar.

The properties of these elusive AGNs are usually explained by two scenarios: (1) heavy obscuration by dust with a large covering factor (Marconi et al. 2000; Fabian 2004; Dudley & Wynn-Williams 1997) and/or (2) a radiatively inefficient accretion flow (RIAF; Yuan & Narayan 2004). Large dust covering factors obscure the optical emission from the inner regions; thus, no narrow

emission lines are observed. The inefficient accretion explains the lack of optical and ultraviolet radiation from the accretion disk and of emission lines from the broad- and narrow-line regions. The existence of unabsorbed XBONGs (Severgnini et al. 2003; Page et al. 2003) in the X-rays disfavors the former hypothesis, although it is likely that both scenarios might be valid. Based on IR and submillimeter observations of some of these elusive AGNs (Borys et al. 2005; Alexander et al. 2005a, 2005b; Martínez-Sansigre et al. 2006), it has been proposed that the obscuring dust is associated with a starburst and that these AGNs might be in an early phase of their growth. These objects might have already formed the bulk of their stellar mass, but the central black hole has not fully grown and they are accreting at a low rate (Alexander et al. 2005b; Borys et al. 2005). This last scenario combines the two described above. In summary, all these classes of AGNs are explained by either heavy absorption associated with dust with a large covering factor, an inefficiently accreting black hole, or both.

We examine in more detail the properties of three SFs for which spectroscopic data are also available and fail in identifying the AGN, XMDS seq. 439, 487, and 842. Our goal is to find out what they have in common that might explain their elusiveness and whether we can identify their AGN activity by other means in absence of X-ray data. All three sources are fitted with spiral templates; however, XMDS seq. 487 shows a small excess of emission in the near-IR with respect to the template. Such an excess is likely due to AGN-heated hot dust. Indeed, a fit with an AGN1 template is one of its secondary solutions. All three sources are absorbed in the X-rays ($N_H \gtrsim 2 \times 10^{22}$ cm^{-2}) and their X-ray luminosities cover a broad range, from $10^{41.5}$ to $10^{44.4}$ erg s^{-1}. The mid-IR/radio luminosity ratios of two sources are consistent with those observed in radio-quiet AGNs and normal galaxies; however, XMDS seq. 439 shows a lower than expected ratio ($\simeq 13.1$, compared to the expected 14.4; see Fig. 12). This low ratio indicates radio emission in excess, and thus strongly suggests AGN activity. In summary, by using the mid-IR/radio luminosity ratio and the secondary solutions of the SED fits, we can identify AGN activity in two of these three sources. The AGN nature of the third source, XMDS seq. 842, is actually not confirmed (see §§ 3.3 and 9).

Overall, we do not find any evidence for inefficient accretion in SFs. Indeed, they could be intrinsically powerful X-ray sources, and their X-ray/radio luminosity ratios satisfy the same correlations observed for AGN1s and AGN2s. The results from this study on these sources favor obscuration as the cause of the observed low mid-IR/X-ray luminosity ratios and elusive SEDs. However, an analysis of a larger sample with a broad range of luminosities and a rich multiwavelength data set and, especially, more discriminating model predictions for various dust distributions and orientations, linked with the X-ray properties, are necessary to investigate whether our results are simply consistent with an orientation effect, or indicate higher dust covering factors or larger dust inner radii.

10.3. The Missing AGN Population

The cosmic X-ray background is still unresolved at high energies (≥ 10 keV). The most recent background synthesis models predict that the missing population is made of sources at intermediate redshifts ($z \sim 1$), with hard X-ray spectra ($\Gamma \sim 1.4$) and moderate luminosities ($\sim 10^{43}$ erg s^{-1}; Worsley et al. 2005; Gilli et al. 2007). Simpson et al. (2006) suggest that the missing AGN population would be detected at radio wavelengths with fluxes of a few tens of microjanskys. The expected radio luminosity of an AGN with an X-ray luminosity of 10^{43} erg s^{-1} derived using the correlation shown in Figure 13 is about 10^{29} erg s^{-1} Hz^{-1}.

The observed radio flux, assuming a redshift of 1 as predicted for the bulk of this missing AGN population, would be $\simeq 2.2$ μJy and the observed 0.5–10 keV X-ray flux would be $\simeq 2.35 \times 10^{-15}$ erg cm^{-2} s^{-1} if unobscured and reduced by 20%, 50%, or 80% if obscured by a column density of 10^{22}, 10^{23}, or 10^{24} cm^{-2}, respectively. The predicted radio fluxes are lower than the limits reached by the deepest radio surveys. Indeed, the rms of the deepest VLA surveys is 2.7 μJy in the 0.4 deg^2 SWIRE-*Chandra* field (Polletta et al. 2006; F. Owen & G Morrison 2007, in preparation) and 5.3 μJy in the 0.04 deg^2 GOODS-North field (Morrison et al. 2007). Thus, the faint radio population is not a good candidate for the missing AGN population. Similar conclusions have been recently derived from stacking the X-ray data of faint radio-selected sources in Hubble Deep Field–North (Barger et al. 2007).

11. SUMMARY

Using the large data set from the XMM-LSS, SWIRE, CFHTLS, and VVDS surveys in the XMDS field (Paper I), the properties (SEDs, luminosity, and absorption) of a hard X-ray selected sample of 136 X-ray sources are investigated. Photometric redshifts are estimated and spectral types are determined using the HYPERZ code and a library of galaxy and AGN templates using optical and infrared data (§ 3). In this work, we investigate the role of the main parameters responsible for the observed properties of AGN SEDs, host-galaxy contribution, gas obscuration, dust absorption, and AGN power. Our analysis is based on multiwavelength data, on the characterization of the average SEDs, and on the comparison of the luminosities emitted in the main energy windows, optical, mid-IR, X-rays, and radio. Of 136 hard X-ray sources, 132 are AGNs, two are clusters, and two are star-forming galaxies. From the AGN sample, we select a subsample of 117 AGNs with high-quality SEDs. The main results obtained from the analysis of this sample are summarized below.

AGN SED classification.—We fit the optical-IR (from 0.37 to 24 μm) SEDs of the whole sample (134 sources, excluding the two clusters) to estimate photometric redshifts and classify the sources. Spectroscopic data are available for 33 sources. We obtain photometric redshifts with $\sigma(1 + z) = 0.11$ and 6% of outliers. The AGN sample is divided in three classes based on their SEDs, type 1 AGNs (AGN1, 33^{+6}_{-1}%), type 2 AGNs (AGN2, 50^{+6}_{-11}%), and star-forming-galaxy–like AGNs (SF, 17^{+9}_{-6}%; § 3.1).

Average SEDs.—We derive average SEDs, from hard X-ray to mid-IR wavelengths, for each AGN class (§ 4). AGN1s show AGN-dominated SEDs from optical to IR wavelengths and mostly unabsorbed X-ray spectra. Their optical spectra show a broad range of extinction, up to $A_V = 0.55$, indicating that the AGN1 class includes some reddened AGNs. In AGN2s, hot dust emission associated with the AGN is detected at mid-IR wavelengths, and emission from the host galaxy dominates in the optical. They show a broad range of X-ray properties, with the majority being absorbed in the X-rays. Sources classified as SFs do not show any AGN signature at optical and IR wavelengths; they are all absorbed in the X-rays.

Average SEDs versus X-ray luminosity and SED class.—The change in the average SEDs per class as a function of X-ray luminosity is analyzed in § 7. The comparison of the average SEDs of each class shows that the optical-IR SEDs in the AGN2 and SF classes and the IR SEDs in the AGN1 class redden as the luminosity increases. This reddening is consistent with a lower relative contribution from the host galaxy to the near-IR luminosity at larger X-ray luminosities.

X-ray versus IR luminosity.—The majority of sources with high X-ray luminosities are AGN1s, while SFs dominate at lower luminosities. No correlation is observed between the X-ray or mid-IR luminosity and the X-ray absorption. We compare the mid-IR (3–20 μm) over absorption-corrected X-ray luminosity ratio with the X-ray luminosity and with observed values from various AGN samples in the literature. The luminosity ratios are characterized by a wide dispersion as are the sources in the literature and we do not find any dependence on the X-ray luminosity. However, we find sources with significantly lower ratios in the SF class. Even lower ratios are found for submillimeter-detected AGNs. These low ratios are explained by either obscuration in the mid-IR or lack of hot dust as expected if the dust is located at a relatively large distance, e.g., 10 pc, from the central heating source (Ballantyne et al. 2006). However, other explanations cannot be ruled out with the present data.

AGN mid-IR colors.—The analysis of AGN red mid-IR colors as measured by IRAC reveals that redness is strongly correlated with the AGN class but also with the X-ray and mid-IR luminosities and does not depend on the X-ray absorption (§ 8). The correlation of the mid-IR redness with the AGN class is likely due to a decreasing host-galaxy contribution from SFs to AGN1s.

Radio luminosity versus X-ray and IR luminosities.—Radio luminosities are compared with the X-ray and mid-IR luminosities, confirming previously known relationships (Brinkmann et al. 2000; Sopp & Alexander 1991) for AGNs (§ 9). A subset of sources show radio emission in excess of the optical and/or mid-IR flux, consistent with being radio-intermediate. We propose the use of the radio luminosity to identify heavily obscured AGNs by estimating the unabsorbed X-ray luminosity in radio-quiet AGNs and by comparing the estimated flux with the observed X-ray flux.

AGN identification through SED fitting.—The SED fitting technique presented here succeeds in identifying AGN signatures in 83% of the objects in the hard X-ray sample. The remaining 17^{+9}_{-6}% of AGNs are fitted with star-forming galaxy templates (SF class). A comparison with the spectroscopic classification available for a small subsample indicates that the AGN1 class is 100% reliable and 62% complete. The AGN2 class is 29% reliable and 58% complete, and the SF class is 33% reliable and 27% complete. The SED and the spectroscopic classification agree in 53% of the cases.

The nature of elusive AGNs.—AGNs in the SF class are elusive AGNs at optical and IR wavelengths, similar to optically dull AGNs, XBONGs, and type 3 QSOs. The properties of these sources can be simply explained by large obscuration in the mid-IR, but it is not clear whether the large obscuration is an effect of orientation or whether it implies larger covering factors and/or dust at a larger distance from the nucleus. We do not find any evidence for inefficient accretion in these sources as they can be powerful X-ray sources.

The missing AGN population.—We investigated whether the AGNs still missing from X-ray surveys and responsible for the bulk of the CXRB at high energies (10–30 keV) can be detected at radio wavelengths. The expected radio flux, derived assuming an X-ray luminosity of 10^{43} erg s^{-1}, the relationship shown in Figure 13, and $z = 1$, is $\sim$2.2 μJy. This flux density is lower than the limits reached by the deepest current radio surveys. Thus, they will still be missing even in radio surveys.

The SED analysis of the AGN sample presented here indicates the existence of a large fraction of AGNs that would remain unidentified in optical- and/or IR-selected samples (SFs). These elusive AGNs show a broad range of luminosities and are mostly X-ray absorbed. The evolution of this population needs to be constrained and taken into account in all evolutionary models. In backward evolutionary models, where SEDs are associated with different types of sources (Xu et al. 2001, 2003; Silva et al. 2004; Treister & Urry 2005), the inclusion of AGNs with an SF SED will greatly affect the estimated contribution of AGNs at all wavelengths, especially in the mid-IR, where AGN-dominated SEDs are much redder than SF SEDs. The identification of these objects would be important in estimating the contribution of accretion energy to the mid-IR background and source counts (Silva et al. 2004; Treister et al. 2006; Ballantyne et al. 2006).

REFERENCES

Akiyama, M., Ueda, Y., Ohta, K., Takahashi, T., & Yamada, T. 2003, ApJS, 148, 275
Akylas, A., Georgantopoulos, I., Georgakakis, A., Kitsionas, S., & Hatziminaoglou, E. 2006, A&A, 459, 693
Alexander, D. M., Aussel, H., Bauer, F. E., Brandt, W. N., Hornschemeier, A. E., Vignali, C., Garmire, G. P., & Schneider, D. P. 2002, ApJ, 568, L85
Alexander, D. M., Bauer, F. E., Chapman, S. C., Smail, I., Blain, A. W., Brandt, W. N., & Ivison, R. J. 2005a, ApJ, 632, 736
Alexander, D. M., Brandt, W. N., Hornschemeier, A. E., Garmire, G. P., Schneider, D. P., Bauer, F. E., & Griffiths, R. E. 2001a, AJ, 122, 2156
Alexander, D. M., Smail, I., Bauer, F. E., Chapman, S. C., Blain, A. W., Brandt, W. N., & Ivison, R. J. 2005b, Nature, 434, 738
Alexander, D. M., et al. 2001b, ApJ, 554, 18
Alonso-Herrero, A., Ward, M. J., & Kotilainen, J. K. 1997, MNRAS, 288, 977
Appleton, P. N., et al. 2004, ApJS, 154, 147

Arnaud, K. A. 1996, in ASP Conf. Ser. 101, Astronomical Data Analysis Software and Systems V, ed. G. H. Jacoby & J. Barnes (San Francisco: ASP), 17

Babbedge, T. S. R., et al. 2004, MNRAS, 353, 654

Ballantyne, D. R., Shi, Y., Rieke, G. H., Donley, J. L., Papovich, C., & Rigby, J. R. 2006, ApJ, 653, 1070

Barger, A. J., Cowie, L. L., Brandt, W. N., Capak, P., Garmire, G. P., Hornschemeier, A. E., Steffen, A. T., & Wehner, E. H. 2002, AJ, 124, 1839

Barger, A. J., Cowie, L. L., Mushotzky, R. F., & Richards, E. A. 2001, AJ, 121, 662

Barger, A. J., Cowie, L. L., & Wang, W. 2007, ApJ, 654, 764

Barmby, P., et al. 2006, ApJ, 642, 126

Bassani, L., Dadina, M., Maiolino, R., Salvati, M., Risaliti, G., della Ceca, R., Matt, G., & Zamorani, G. 1999, ApJS, 121, 473

Bassani, L., et al. 2006, ApJ, 636, L65

Beckmann, V., Gehrels, N., Shrader, C. R., & Soldi, S. 2006, ApJ, 638, 642

Berta, S. 2005, Ph.D. thesis, Univ. Padua

Berta, S., Fritz, J., Franceschini, A., Bressan, A., & Pernechele, C. 2003, A&A, 403, 119

Bolzonella, M., Miralles, J.-M., & Pelló, R. 2000, A&A, 363, 476

Bondi, M., et al. 2003, A&A, 403, 857

Borys, C., Smail, I., Chapman, S. C., Blain, A. W., Alexander, D. M., & Ivison, R. J. 2005, ApJ, 635, 853

Brandl, B. R., et al. 2006, ApJ, 653, 1129

Brandt, W. N., et al. 2001, AJ, 122, 2810

Brinkmann, W., Laurent-Muehleisen, S. A., Voges, W., Siebert, J., Becker, R. H., Brotherton, M. S., White, R. L., & Gregg, M. D. 2000, A&A, 356, 445

Brodwin, M., et al. 2006, ApJ, 651, 791

Bruzual, A. G., & Charlot, S. 2003, MNRAS, 344, 1000

Calzetti, D., Armus, L., Bohlin, R. C., Kinney, A. L., Koornneef, J., & Storchi-Bergmann, T. 2000, ApJ, 533, 682

Chiappetti, L., et al. 2005, A&A, 439, 413 (Paper I)

Ciliegi, P., et al. 2005, A&A, 441, 879

Colbert, E. J. M., Heckman, T. M., Ptak, A. F., Strickland, D. K., & Weaver, K. A. 2004, ApJ, 602, 231

Coleman, G. D., Wu, C.-C., & Weedman, D. W. 1980, ApJS, 43, 393

Comastri, A., et al. 2002, preprint (astro-ph/0203019)

Condon, J. J., & Broderick, J. J. 1988, AJ, 96, 30

de Jong, T., Klein, U., Wielebinski, R., & Wunderlich, E. 1985, A&A, 147, L6

Devriendt, J. E. G., Guiderdoni, B., & Sadat, R. 1999, A&A, 350, 381

Dickey, J. M., & Salpeter, E. E. 1984, ApJ, 284, 461

Donley, J. L., Koribalski, B. S., Staveley-Smith, L., Kraan-Korteweg, R. C., Schröder, A., & Henning, P. A. 2006, MNRAS, 369, 1741

Donley, J. L., Rieke, G. H., Rigby, J. R., & Pérez-González, P. G. 2005, ApJ, 634, 169

Dudley, C. C., & Wynn-Williams, C. G. 1997, ApJ, 488, 720

Dye, S., et al. 2006, ApJ, 644, 769

Eckart, M. E., Stern, D., Helfand, D. J., Harrison, F. A., Mao, P. H., & Yost, S. A. 2006, ApJS, 165, 19

Elvis, M., Schreier, E. J., Tonry, J., Davis, M., & Huchra, J. P. 1981, ApJ, 246, 20

Elvis, M., et al. 1994, ApJS, 95, 1

Fabian, A. C. 2004, in Coevolution of Black Holes and Galaxies, ed. L. C. Ho (Cambridge: Cambridge Univ. Press), 446

Fadda, D., Flores, H., Hasinger, G., Franceschini, A., Altieri, B., Cesarsky, C. J., Elbaz, D., & Ferrando, Ph. 2002, A&A, 383, 838

Fioc, M., & Rocca-Volmerange, B. 1997, A&A, 326, 950

Franceschini, A., et al. 2005, AJ, 129, 2074

Garcet O., et al. 2007, A&A, submitted

Gavignaud, I., et al. 2006, A&A, 457, 79

Giacconi, R., et al. 2002, ApJS, 139, 369

Gilli, R., Comastri, A., & Hasinger, G. 2007, A&A, 463, 79

Glikman, E., Gregg, M. D., Lacy, M., Helfand, D. J., Becker, R. H., & White, R. L. 2004, ApJ, 607, 60

Granato, G. L., & Danese, L. 1994, MNRAS, 268, 235

Granato, G. L., Danese, L., & Franceschini, A. 1997, ApJ, 486, 147

Gregg, M. D., Lacy, M., White, R. L., Glikman, E., Helfand, D., Becker, R. H., & Brotherton, M. S. 2002, ApJ, 564, 133

Hasinger, G. 2002, Rev. Mod. Astron., 15, 71

Hatziminaoglou, E., et al. 2005, AJ, 129, 1198

Higdon, J. L., et al. 2005, ApJ, 626, 58

Horst, H., Smette, A., Gandhi, P., & Duschl, W. J. 2006, A&A, 457, L17

Ilbert, O., et al. 2006, A&A, 457, 841

Jarrett, T. H., et al. 2006, AJ, 131, 261

Kim, D.-W., Fabbiano, G., & Trinchieri, G. 1992a, ApJS, 80, 645

———. 1992b, ApJ, 393, 134

Kitsionas, S., Hatziminaoglou, E., Georgakakis, A., & Georgantopoulos, I. 2005, A&A, 434, 475

Lacy, M., Petric, A. O., Sajina, A., Canalizo, G., Storrie-Lombardi, L. J., Armus, L., Fadda, D., & Marleau, F. R. 2007, AJ, 133, 186

Lacy, M., et al. 2004, ApJS, 154, 166

Lawrence, A. 1991, MNRAS, 252, 586

Lawrence, J. F., Shearer, P. M., & Masters, G. 2006, Geophys. Res. Lett., 33, L07315

Le Fèvre, O., et al. 2004, A&A, 417, 839

———. 2005, A&A, 439, 845

Leipski, C., et al. 2007, A&A, 464, 895

Lonsdale, C., et al. 2004, ApJS, 154, 54

Lonsdale, C. J., et al. 2003, PASP, 115, 897

Lutz, D., Maiolino, R., Spoon, H. W. W., & Moorwood, A. F. M. 2004, A&A, 418, 465

Maiolino, R., Salvati, M., Bassani, L., Dadina, M., della Ceca, R., Matt, G., Risaliti, G., & Zamorani, G. 1998, A&A, 338, 781

Maiolino, R., et al. 2003, MNRAS, 344, L59

Marconi, A., Oliva, E., van der Werf, P. P., Maiolino, R., Schreier, E. J., Macchetto, F., & Moorwood, A. F. M. 2000, A&A, 357, 24

Martínez-Sansigre, A., Rawlings, S., Lacy, M., Fadda, D., Jarvis, M. J., Marleau, F. R., Simpson, C., & Willott, C. J. 2006, MNRAS, 370, 1479

McCracken, H. J., et al. 2003, A&A, 410, 17

Moran, E. C., Filippenko, A. V., & Chornock, R. 2002, ApJ, 579, L71

Morrison, G., et al. 2007, in ASP Conf. Ser., The Spitzer Science Center 2005 Conference: Infrared Diagnostics of Galaxy Evolution, ed. R.-R. Chary (San Francisco: ASP), in press (astro-ph/0603412)

Mulchaey, J. S., Koratkar, A., Ward, M. J., Wilson, A. S., Whittle, M., Antonucci, R. R. J., Kinney, A. L., & Hurt, T. 1994, ApJ, 436, 586

Page, M. J., et al. 2003, Astron. Nachr., 324, 101

Perola, G. C., et al. 2004, A&A, 421, 491

Persic, M., Rephaeli, Y., Braito, V., Cappi, M., Della Ceca, R., & Franceschini, A., & Gruber, D. E. 2004, A&A, 419, 849

Pierre, M., et al. 2004, J. Cosmol. Astropart. Phys., 9, 11

———. 2007, MNRAS, submitted

Polletta, M., et al. 2006, ApJ, 642, 673

Ranalli, P., Comastri, A., & Setti, G. 2003, A&A, 399, 39

Rigby, J. R., Rieke, G. H., Donley, J. L., Alonso-Herrero, A., & Pérez-González, P. G. 2006, ApJ, 645, 115

Rigby, J. R., Rieke, G. H., Pérez-González, P. G., Donley, J. L., Alonso-Herrero, A., Huang, J.-S., Barmby, P., & Fazio, G. G. 2005, ApJ, 627, 134

Risaliti, G., Maiolino, R., & Salvati, M. 1999, ApJ, 522, 157

Rosati, P., et al. 2002, ApJ, 566, 667

Rowan-Robinson, M., et al. 2005, AJ, 129, 1183

Roy, A. L., Norris, R. P., Kesteven, M. J., Troup, E. R., & Reynolds, J. E. 1998, MNRAS, 301, 1019

Sanders, D. B., Phinney, E. S., Neugebauer, G., Soifer, B. T., & Matthews, K. 1989, ApJ, 347, 29

Schmidt, M., & Green, R. F. 1983, ApJ, 269, 352

Severgnini, P., et al. 2003, A&A, 406, 483

Silva, L., Granato, G. L., Bressan, A., & Danese, L. 1998, ApJ, 509, 103

Silva, L., Maiolino, R., & Granato, G. L. 2004, MNRAS, 355, 973

Simpson, C., Rawlings, S., & Martínez-Sansigre, A. 2006, Astron. Nachr., 327, 270

Sopp, H. M., & Alexander, P. 1991, MNRAS, 251, 14P

Spergel, D. N., et al. 2003, ApJS, 148, 175

Stern, D., et al. 2004, ApJ, 612, 690

Stocke, J. T., Morris, S. L., Weymann, R. J., & Foltz, C. B. 1992, ApJ, 396, 487

Sturm, E., Hasinger, G., Lehmann, I., Mainieri, V., Genzel, R., Lehnert, M. D., Lutz, D., & Tacconi, L. J. 2006, ApJ, 642, 81

Szokoly, G. P., et al. 2004, ApJS, 155, 271

Tajer, M., et al. 2007, A&A, in press (Paper II)

Treister, E., & Urry, C. M. 2005, ApJ, 630, 115

Treister, E., et al. 2004, ApJ, 616, 123

———. 2006, ApJ, 640, 603

Turner, T. J., George, I. M., Nandra, K., & Mushotzky, R. F. 1997, ApJ, 488, 164

Ueda, Y., Akiyama, M., Ohta, K., & Miyaji, T. 2003, ApJ, 598, 886

Urrutia, T., Lacy, M., Gregg, M. D., & Becker, R. H. 2005, ApJ, 627, 75

Virani, S. N., et al. 2005, BAAS, 37, 1190

Weedman, D., et al. 2006, ApJ, 653, 101

Wilkes, B. J., & Elvis, M. 1987, ApJ, 323, 243

Wilkes, B. J., Pounds, K. A., Schmidt, G. D., Smith, P. S., Cutri, R. M., Ghosh, H., Nelson, B., & Hines, D. C. 2005, ApJ, 634, 183

Wilkes, B. J., Schmidt, G. D., Cutri, R. M., Ghosh, H., Hines, D. C., Nelson, B., & Smith, P. S. 2002, ApJ, 564, L65

Worsley, M. A., et al. 2005, MNRAS, 357, 1281

Xu, C., Lonsdale, C. J., Shupe, D. L., O'Linger, J., & Masci, F. 2001, ApJ, 562, 179

Xu, C. K., Lonsdale, C. J., Shupe, D. L., Franceschini, A., Martin, C., & Schiminovich, D. 2003, ApJ, 587, 90

Yuan, F., & Narayan, R. 2004, ApJ, 612, 724